Numerical Investigation of a Radially Cooled Turbine Guide Vane Using Air and Steam as a Cooling Medium

Sondre Norheim

University of Bergen
Geophysical institute

Western Norway University of Applied Sciences
Department of Mechanical- and Marine Engineering

Bergen, May 2021

Supervisors:
Dr. Shokri Amzin
Dr. Bjørn Arntzen

University of Bergen (UiB)
The Faculty of Mathematics and Natural Sciences
Geophysical Insitute
Post Box 7803
5020 Bergen, Norway

In cooperation with:
Western Norway University of Applied Sciences (HVL)
The Faculty of Engineering and Sciences
Department of Mechanical and Marine Engineering (IMM)
Post Box 7030
5020 Bergen, Norway

Author: Sondre Norheim
Student number: 181342

Program: Master Programme in Energy, Thermal Machines
Course: ENERGI
Credits: 30 ECTS
Date: May 2021
Supervisor: Associate Professor Shokri Amzin
Supervisor: Professor Bjørn Arntzen

Working files submitted: 2

Preface

This 30 ECTS master thesis was written as part of the master's programme in Energy with specialisation in Thermal Machines. The programme is a cooperation between the Department of Mechanical- and Marine Engineering at Western Norway University of Applied Sciences and University of Bergen. The thesis was carried out during the winter and spring of 2021, and was somewhat affected by the COVID-19 pandemic. Regardless of the affects, the process was highly educative and interesting.

I would like to acknowledge and express my deepest gratitude to the following people for their support and assistance during the project:

A special thanks to my supervisor at Western Norway University of Applied Sciences, Dr. Shokri Amzin. Without his guidance, knowledge and persistent support during all stages, the project would not have been possible. I would like to thank him for introducing me to the field of computational fluid dynamics. I also appreciate his dedication and enthusiasm during my education at HVL.

Thanks to Dr. Bjørn Arntzen for his contribution to the structure and the scientific writing of the thesis.

I would also like to thank Dr. Boris Balakin for giving me the opportunity to work with the CFD software STAR CCM+.

Finally, a special thanks to my family and friends for their continuous motivational support.

Bergen, May 2021.
Sondre Norheim

Publications from this work

S.Norheim and S.Amzin, "Numerical Investigation of a Radially Cooled Turbine Guide Vane Using Air and Steam as a Cooling Medium," *Multidisciplinary Digital Publishing Institute, Computations*, 2021 - https://doi.org/10.3390/computation9060063

Previous publications

B. Haugen, B. Rødland, S. Norheim, H. Momeni and S. Amzin, "Numerical Modelling of Two-Phase Flow in a Gas Separator Using the Eulerian–Lagrangian Flow Model," *Journal of Engineering*, vol. 2021 - https://doi.org/10.1155/2021/4385904

Abstract

Gas turbine performance is closely linked to the turbine inlet temperature, which in turn is limited by the turbine guide vanes ability to withstand the massive thermal loads. To improve the efficiency in modern high-temperature gas turbines, steam cooling has been introduced as a new advanced cooling technique. This study compares the cooling performance of compressed air and steam in the renowned radially cooled NASA C3X turbine guide vane, using a numerical model. The conjugate heat transfer (CHT) model is based on the RANS-method, where the shear stress transport (SST) $k-\omega$ model is selected to predict the effects of turbulence. The numerical model is validated against experimental pressure and temperature distributions at the external surface of the vane, where air is used as coolant. The results are in good agreement with the experimental data, with an average error of 1.39% and 3.78%, respectively. By comparing the numerical simulations of the two coolants, steam is confirmed as the superior cooling medium. The disparity between the coolants increases along the axial direction of the vane, and the total volume average temperature difference is 30 K. Further investigations are recommended to deal with the local hot-spots located near the leading- and trailing edge of the vane.

Table of contents

List of figures **xi**

List of tables **xii**

Nomenclature **xiii**

1 Introduction **1**
1.1 Objectives 3

2 Background on gas turbines **4**
2.1 History of gas turbines 4
2.2 Working principle 5
2.3 Turbine vane cooling 7

3 Turbulent flow modelling **9**
3.1 General formulations of the governing equations 9
3.1.1 Conservation of mass 9
3.1.2 Conservation of momentum 9
3.1.3 Conservation of energy 10
3.1.4 State equation 11
3.2 Numerical approaches 11
3.2.1 DNS - Direct numerical simulation 11
3.2.2 Large eddy simulation 12
3.2.3 Reynolds Averaged Navier Stokes 13
3.2.4 Detached eddy simulation 13
3.3 Turbulent flow modelling 14
3.3.1 Favre filtered governing equations 14
3.3.2 Turbulence modelling 15

4 Experimental and numerical details 18
4.1 Experimental details 18
4.2 Physics models 21
4.3 Initial conditions 22
4.4 Boundary conditions 23
4.5 Computational mesh 25
4.6 Hardware 27
4.7 Mesh independence 28
4.8 Convergence 29

5 Results and discussion 30
5.1 Model validation 30
5.1.1 Aerodynamic characteristics 30
5.1.2 Temperature distribution 34
5.2 Comparison of air and steam 36

6 Summary and conclusion 41

References 42

List of figures

2.1 Schematic of the ideal Brayton-cycle. 5
2.2 Evolution of cooling techniques for turbine guide vanes. 7
2.3 Typical configuration of a modern turbine guide vane. 8

4.1 Schematic of the NASA C3X vane with enumerated cooling channel. . . . 19
4.2 Computational domain used in the simulations. 19
4.3 Depiction of a conformal and non-conformal mesh. 25
4.4 Schematic of the generated mesh in the X-Y plane, with detailed representation of the leading and trailing edge of the vane. 27
4.5 Mesh independence test. 28
4.6 Residuals monitor plot. 29
4.7 Volume average temperature plot. 29

5.1 Comparison of the normalised static pressure from the experimental report and the numerical simulations at mid-span. 30
5.2 Contours of the Mach number on the mid-span plane, including enlarged views of the transition regions on the suction side and near the trailing edge. 31
5.3 Numerical Schlieren and shadowgraph image of the flow over the C3X vane. 32
5.4 Comparison of the normalised temperature from the experimental report and the numerical simulations at mid-span. 34
5.5 Normalised temperature distribution along a straight line at mid-span, which cuts through all computational regions at hole number 3. 35
5.6 Location of the three cross-sectional planes used for comparison. 36
5.7 Comparison of normalised temperature distribution at the three cross-sectional planes. 37
5.8 Temperature contour comparison of the different cross-sectional planes. . . 38
5.9 Temperature contour comparison of the suction and pressure side. 40

List of tables

3.1 Model coefficients 17

4.1 Geometric parameters of C3X vane 18
4.2 Selected physics models for the hot and cold fluids 21
4.3 Selected physics models for the C3X vane 21
4.4 Initial conditions of the regions 22
4.5 Boundary conditions of the external gas stream 23
4.6 Boundary conditions of the cooling channels used for both air and steam . . 23
4.7 Sutherland constants for air and steam 24
4.8 Constants for polynomial specific heat capacity 24
4.9 Global mesh settings 26
4.10 Prism layer settings for the cooling channels and the vane external surface . 26
4.11 Hardware specifications of the computer 27

Nomenclature

Roman Symbols

c_p	Specific heat capacity
d	Distance
D_h	Hydraulic diameter
E	Total energy
e_m	Kinetic energy
e_t	Thermal energy
F_i	Body force
G	Filtering function
h	Enthalpy
k	Turbulent kinetic energy
K_g	Thermal conductivity of gas
K_s	Thermal conductivity of solid
L	Length scale
$\dot{M}$	Mass flow rate
N	Number of grid points
p	Pressure
Pr	Prandtl number (Dimensionless)

q	Energy in form of heat
R	Universal gas constant
Re	Reynolds number (Dimensionless)
S_{ij}	Rate of strain tensor
S_R	Radiation source term
T	Temperature
t	Time
T_t	Turbulent time scale
T_u	Turbulence intensity
T_v	Turbulence viscosity ratio
u	Velocity component
u_τ	Friction velocity
W	Work
y	Absolute wall distance
y^+	Dimensionless wall distance

Greek Symbols

Δ_x	Grid spacing
δ_{ij}	Kronecker delta; δ_{ij} = 1 if i=j, and 0 otherwise
η_k	Kolmogorov length scale
λ	Thermal conductivity
μ	Dynamic viscosity
μ_t	Turbulent viscosity
η_{th}	Thermal efficiency
ν	Kinematic viscosity

ω	Specific dissipation rate
$\bar{\phi}$	Averaged flow variable
ϕ	Arbitrary flow variable
ϕ'	Fluctuating flow variable
ϕ''	Fluctuating flow variable
$\tilde{\phi}$	Favre averaged flow variable
ρ	Density of a substance
Δ_t	Time step
τ_{ij}	Shear-stress tensor

Subscripts

i	Direction along an axis
j	Direction perpendicular to i
t	Turbulent

Acronyms / Abbreviations

CFD	Computational fluid dynamics
CHT	Conjugate heat transfer
CO_2	Carbon dioxide
RAM	Central processing unit
DES	Detached eddy simulation
DNS	Direct numerical simulation
H_2O	Water/steam
LE	Leading edge
LES	Large eddy simulation
LHS	Left hand side

PS	Pressure side
RAM	Random access memory
RANS	Reynolds-averaged Navier-Stokes
RHS	Right hand side
SGS	Subgrid-scale
NO_x	Nitrogen oxides
SS	Suction side
SST	Shear stress transport
TE	Trailing edge
TIT	Turbine inlet temperature
WW2	Second world war

Chapter 1

Introduction

Ever since mankind discovered energy in the form of fire, it has constantly been evolving. In the beginning, the energy was primarily used for heating purposes, but eventually, humankind discovered other ways of utilising it. By harnessing the energy from wind and water, the human population was able to increase and spread across the globe.

The emergence of the industrial revolution in the eighteenth- and nineteenth centuries brought significant advancements in harnessing energy. The invention of the steam engine in 1769 sparked the beginning of a new era in technology and innovation. Then followed the invention Diesel engine, by Rudolf Diesel in 1898. These inventions made it possible to convert thermal energy into mechanical energy, by utilising the energy from combustion of fossil fuels. This revolutionised the industry and transport sector, and as a consequence, the demand for fossil fuels increased to the current levels.

Although fossil fuels are a crucial element in combustion, it is considered to be harmful to both the environment and humankind. It is widely acknowledged that combustion of fossil fuels could lead to an increase in the average global temperature [1]. This phenomenon is also recognised as global warming. Greenhouse gases like carbon dioxide (CO2), and water (H2O), trap the heat from the sun in the atmosphere, and the global temperature increases. Coincidentally, CO2 and H2O are two major products from combustion of fossil fuels. Other products include sulphur oxide (SO2) and nitrogen oxides (NOx), which also introduces some unwanted effects [2, 3]. As a result, more stringent legislations have been endorsed to decrease the environmental impact of combustion.

Growing awareness of global warming and increasingly stringent regulations has led to a shift in the global energy market. This involves increased production of energy from renewables, like solar, wind and hydropower. Although the production of renewable energy is increasing, it accounted for only 14 % of the global energy market in 2019, while energy from fossil fuels accounted for 80 % [4]. Therefore, it is highly unlikely that renewable

energy would be able to replace fossil fuels in the near future. Thus, in order to reduce the emissions of greenhouse gases, it is necessary to improve the efficiency of the already existing combustion systems.

One of the most widely used combustion systems is the gas turbine, which plays a preeminent role in aviation and energy production [5, 6]. The gas turbines are classified as continuous combustion systems and are based on the ideal Brayton-cycle. The cycle involves isentropic compression and expansion, as well as isobaric (constant pressure) heat addition and rejection. The real cycle involves different losses like mechanical, aerodynamical, heat release and pressure drop, which reduces the efficiency. Therefore, it is desirable to minimise these losses.

Among the most influential parameters in regard to the efficiency is the turbine inlet temperature (TIT) [7]. This temperature is constrained by the turbine vanes and blades ability to withstand the arduous operating conditions. In modern gas turbines, these components are pushed to the limit of what the materials can endure, withstanding temperatures up to 1700 °C [8]. Sophisticated cooling techniques are required to ensure that the blades and vanes can function under the immense thermal loads [9]. Small variations in the inlet temperature could have a significant impact on the lifespan of these components [10]. Therefore, it is critical to have adequate tools to predict the heat transfer mechanism in the vanes, so that the design can be optimised.

Due to the complexity of gas turbines, it is difficult to obtain experimental results on these effects. Although Hylton et al. [11, 12] was able to successfully investigate this phenomenon, the contemporary approach is to use computational fluid dynamics (CFD). This is because CFD software is able to provide detailed approximations of complex fluid-flow phenomena, while being more efficient and less expensive than performing physical experiments. With the recent advancements in computer power, CFD has become more accurate, making it an indispensable tool for solving problems involving heat transfer.

Conjugate heat transfer (CHT) analysis is frequently used in CFD to predict the heat transfer mechanism between the hot gas and vane. This is because CHT combines conduction inside a solid body, the convection from a fluid flow and the interaction between them. A coupled aerodynamic and thermal numerical approach for gas turbines was developed by Bohn et al. [13, 14] in the early 1990s. By using the same discretisation and numerical scheme for both the fluid flow and the solid body, the heat flux between the two regions become interchangeable. Thus, information about heat transfer coefficients on the solid surface is redundant, and the temperature distribution in the solid is a direct result of the analysis. The CHT approach has been further validated with a complete 3D simulation on the NASA C3X vane [15]. Furthermore, a comparison of conjugate and nonconjugated heat

transfer has been performed [16]. Subsequently, the CHT method has been established as an important tool for optimisation and design purposes of turbomachinery.

The famous NASA C3X turbine guide vane [11] has been used in numerous studies to investigate different cooling techniques. It has been proved that the location, cross-section and mass flow rate of the cooling arrangements are highly influential on the temperature distribution in the vane [17]. Other studies have included thermal barrier coating, the effects of turbulence intensity and material selection [18, 19]. Recent developments have suggested replacing compressed air with steam, because of the superior heat transfer capabilities. In combined-cycle power plants, steam is easily accessible through the secondary steam turbine, which could be used on closed-loop cooling systems. This would not only increase the turbine efficiency, but also the overall combined-cycle thermal efficiency. Thus, the primary objective of this study is to investigate the effects of replacing compressed air with steam as the coolant in a turbine guide vane.

1.1 Objectives

The primary objective of this study is to investigate if compressed air can be replaced with steam as coolant in a turbine guide vane. More specifically, the objects are:

1. To conduct a CFD analysis on a turbine guide vane using the commercial software STAR CCM+.

2. Validate the results against experimental results.

3. To replace air with steam as cooling medium and compare the effects on the heat distribution in the vane.

Chapter 2

Background on gas turbines

The scope of this chapter is to provide a brief walkthrough of the history and the working principles of gas turbines. Furthermore, the evolution of turbine vane cooling is reviewed.

2.1 History of gas turbines

The history of gas turbines dates back to 1791 when John Barber held the first patent for a turbine engine. In 1872, the first gas turbine engine was designed by Franz Stolze. This was an attempt to make the first working model, but the design could not produce enough power to run on itself. The first major breakthrough was achieved in 1903 when Norwegian scientist Ægidius Elling built a gas turbine that produced enough power to run on its own [20].

This new invention saw little success until 1939, when the company Brown Boveri designed the first gas turbine used for power generation in Switzerland. Following the WW2, gas turbines saw great improvements and were expected to become important in many areas. However, the cost and low thermal efficiencies halted the success of gas turbines. In the 1980s, when natural gas became a popular fuel, gas turbines finally emerged as one of the most important power production systems.

In 1929, Frank Whittle proposed the idea of using gas turbines as jet engines in aviation [21]. Due to lack of funding, this idea was not materialised until 1939, when the first jet aircraft was developed. After WW2, jet engines gained massive popularity and emerged as the preferable choice for aviation purposes. Through research in materials, cooling and aerodynamics, the efficiency of jet engines has increased. As a result, modern jet engines are used in nearly all aviation activities.

With the increasing focus on global warming and efforts to reduce emissions, gas turbines have found increased interest. Although natural gas is the most commonly used fuel, new investigations have proposed to use more clean fuels in gas turbines. This includes hydrogen,

which is regarded as a promising fuel for the future [22]. However, combustion of hydrogen increases moisture in the exhaust gas, thus increasing the heat transfer to the components in the hot-gas path [23]. Therefore, it is vital to improve the cooling techniques in modern gas turbines.

2.2 Working principle

To better understand the importance of the cooling techniques, it is important to introduce the working principles of a gas turbine. It is based on the ideal Brayton-cycle, which is shown schematically in fig. 2.1. As shown, there are four processes involved in the cycle.

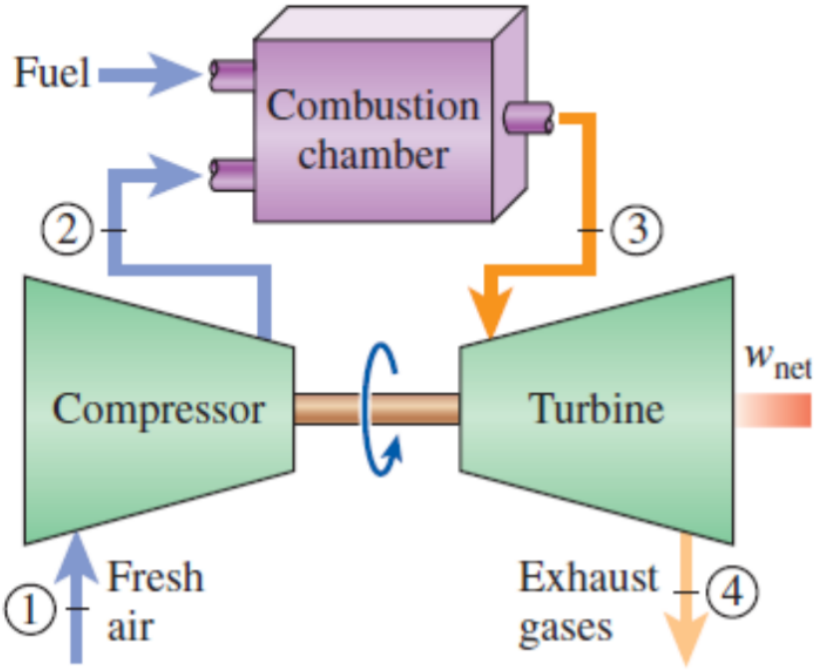

Fig. 2.1 Schematic of the ideal Brayton-cycle [24].

1-2 Isentropic compression (compressor)

2-3 Isobaric heat-addition (combustion)

3-4 Isentropic expansion (turbine)

4-1 Isobaric heat-rejection

As noted, this is an idealised cycle where there are no losses. The isentropic compression and expansion are assumed to be adiabatic and reversible, and the combustion is assumed to be without pressure loss. However, the real cycle deviates due to losses. The compression and expansion are not isentropic and pressure loss occurs in the combustor. In addition, mechanical and aerodynamic losses occur as well.

To evaluate the performance of a gas turbine, the thermal efficiency is frequently used. The efficiency is expressed as

$$\eta_{th,Brayton} = \frac{w_{net}}{q_{in}} = \frac{w_{in} - w_{out}}{q_{in}}, \tag{2.1}$$

where w_{in} is the work added to drive the compressor, w_{out} is the work produced by the turbine, and q_{in} is the energy added to the cycle. All of these terms can be expressed by the enthalpy formulation, which is given as

$$h = c_p(T_2 - T_1). \tag{2.2}$$

By using this formulation in Eq.(2.1), the thermal efficiency $\eta_{th,Brayton}$ is expressed as

$$\eta_{th,Brayton} = \frac{c_p(T_3 - T_4) - c_p(T_4 - T_1)}{c_p(T_3 - T_2)} = 1 - \frac{c_p(T_4 - T_1)}{c_p(T_3 - T_2)}. \tag{2.3}$$

As shown in Eq.(2.3), by increasing T_3, the thermal efficiency would increase. Coincidentally, T_3 is also known as the turbine inlet temperature (TIT). As previously stated, the TIT is restrained by the turbine vanes ability to endure this temperature. Thus, to increase the thermal efficiency, it is necessary to have turbine vanes that can withstand these increasingly large temperatures.

A different approach to raise the thermal efficiency of the Brayton cycle is to increase the compression ratio in the compressor. However, the efficiency growth is limited, and the TIT is dependent on the compressor exit temperature, which increases with higher compression ratios [25]. The more prominent method for increasing the efficiency of gas turbines is to use a regenerative cycle. The heat from the exhaust is used to preheat the air, prior to entering the combustion chamber. This reduces the air/fuel ratio, but also increases the temperature of the combustion. As a result, the turbine inlet temperature is affected. Regardless of the approach, it is evident that the turbine vanes are vital components in a gas turbine.

2.3 Turbine vane cooling

Ever since the first gas turbine, there has been a large interest in increasing the TIT. As a result of the advancements in cooling techniques, the temperature has increased considerably, as shown in fig. 2.2. These advances have increased both the expected lifetime of the components and the efficiency of the gas turbines.

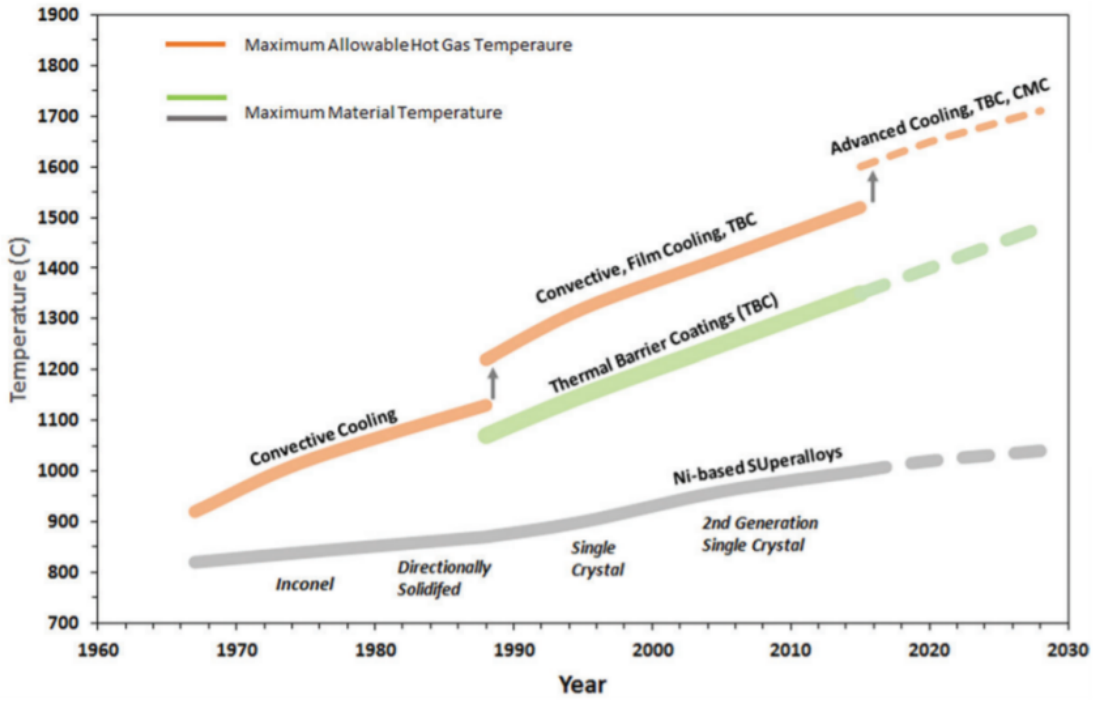

Fig. 2.2 Evolution of cooling techniques for turbine guide vanes [26].

The most basic improvements are in the metallurgical aspects of the vanes. Changing the casting process and the composition of the alloys has increased the durability of the vanes. However, the allowable melting temperature of the materials is increasing slowly, but it is still an important foundation. The introduction of forced convection cooling had a much larger impact on the allowable temperature. Convection cooling is the transfer of heat that occurs from the movement of a fluid. When convection cooling is applied, the turbine vane is heated from the gas stream and cooled internally. In addition, by adding ribs in the convective cooling channels, the area subjected to heat transfer is increased, thus reducing the temperature further.

To deal with the external convection on the turbine vanes, film cooling was introduced. In film cooling, a cool fluid is discharged through small holes on the surface of the object. The cool fluid forms a thin film along the surface of the object, which serves as an insulation

layer. Both the angle and the blow ratio of the holes is influential on the cooling effectiveness [27]. For the same purpose, thermal barrier coating was introduced. By applying a thin layer of refractory-oxide ceramic coating, a thermal barrier is created.

Another notable addition to the cooling techniques used in a turbine vane is jet-impingement. In this technique, an array of high-velocity fluids is forced to collide with a target surface. On the surface, a region with high turbulence is created, which provides a higher heat transfer. Furthermore, by using steam instead of air where applicable, the temperature of the turbine vanes could be cooled even further. In modern-day gas turbines, a combination of all the aforementioned cooling techniques are used, as shown in fig 2.3.

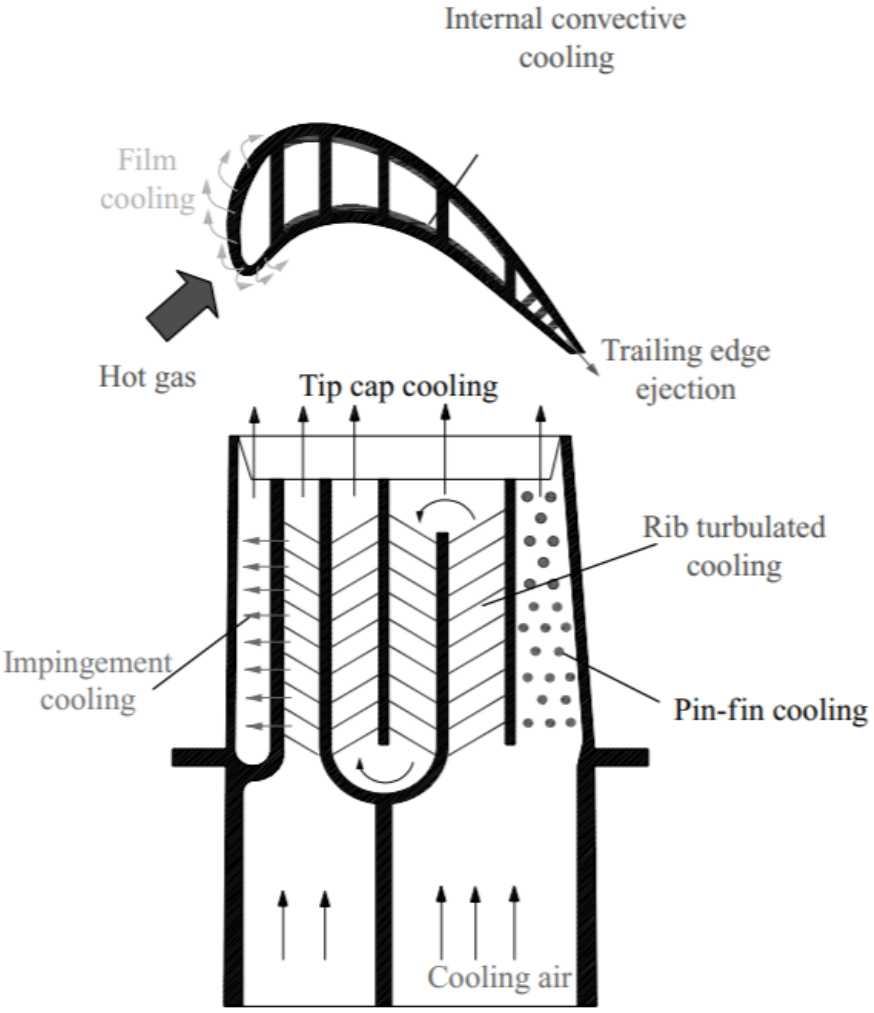

Fig. 2.3 Typical configuration of a modern turbine guide vane [28].

Chapter 3

Turbulent flow modelling

The purpose of this chapter is to give a brief overview of turbulent flow characteristics, and how it is modelled in order to analyse the fluid flow.

The majority of fluid flows are considered to be turbulent. This means that the flow contains irregular fluctuations, and the physical properties of the fluid flow undergo changes in both magnitude and direction. Mathematical models are required to study this phenomenon, and these models are derived from three conservational laws: conservation of mass, momentum, and energy [29]. The three laws of conservation are the foundation for the governing equations in CFD.

3.1 General formulations of the governing equations

3.1.1 Conservation of mass

$$\frac{\partial \rho}{\partial t} + \frac{\partial}{\partial x_i}(\rho u_i) = 0 \tag{3.1}$$

The first term in Eq. (3.1) denote the time variation and the second term denotes the change due to fluid transport inside a control volume. ρ is the density of the fluid, while u is the average velocity.

3.1.2 Conservation of momentum

$$\frac{\partial}{\partial t}(\rho u_i) + \frac{\partial}{\partial x_j}(\rho u_i u_j) = -\frac{\partial p}{\partial x_i} + \frac{\partial \tau_{ij}}{\partial x_j} + F_i \tag{3.2}$$

The first and second term on the left-hand side (LHS) in Eq. (3.2) represents the unsteady term and the rate of change, respectively. On the right-hand side (RHS), the first term denotes the pressure gradient, while the third term denotes the resultant of the body forces.

The second term on RHS represents the momentum due to viscous forces, and τ_{ij} is the shear-stress tensor. The shear-stress tensor can be expressed as

$$\tau_{ij} = 2\mu S_{ij} - \frac{2}{3}\mu\delta_{ij}S_{kk}, \tag{3.3}$$

where μ is the dynamic viscosity, and δ_{ij} is the Kronecker delta. S_{ij} is the rate of strain tensor, which is written as

$$S_{ij} = \frac{1}{2}\left(\frac{\partial u_i}{\partial x_j} + \frac{\partial u_j}{\partial x_i}\right) \tag{3.4}$$

3.1.3 Conservation of energy

To present the energy equation, the energy, e, needs to be defined. The total energy is the sum of kinetic energy and thermal energy and is expressed as

$$E = e_m + e_t, \tag{3.5}$$

where the kinetic and thermal contribution is expressed as

$$e_m = \frac{1}{2}u_i u_i \tag{3.6}$$

$$e_t = \int_{T_{ref}}^{T} C_p(T)dT, \tag{3.7}$$

where C_p is the specific heat capacity, and T is the temperature.

By assuming that there is no contribution from potential or chemical energy, the conservation of energy equation can be written as

$$\frac{\partial}{\partial t}(\rho E) + \frac{\partial}{\partial x_i}(\rho u_i E) = -\frac{\partial}{\partial x_i}(u_i p) + \frac{\partial}{\partial x_i}(u_i \tau_{ij}) - \frac{\partial q_i}{\partial x_i} + S_R. \tag{3.8}$$

The first two terms on the LHS denotes the time derivative of energy and convection term, respectively. On the RHS, the first term represents pressure work, while the second term represents the viscous dissipation. The fourth term describes the radiative heat exchange. The third term represents the heat flux, which is expressed by Fourier's law of conduction [30].

$$q_i = -\lambda\frac{\partial T}{\partial x_i} = -C_p\frac{\mu}{Pr}\frac{\partial T}{\partial x_i} \tag{3.9}$$

where Pr is the dimensionless Prandtl number.

3.1.4 State equation

In order to close these equations, the properties need to be linked together using a specified equation of state,

$$p = \rho RT \tag{3.10}$$

where R is the gas constant.

3.2 Numerical approaches

In the simulation of turbulent flows, the governing equations above are solved. Additional models may be required, depending on the chosen methodology. As briefly mentioned in chapter 1, there are different methods for solving these equations. The most commonly used methods are direct numerical simulation (DNS), large eddy simulation (LES) or Reynolds-averaged Navier-Stokes (RANS). Another method worth mentioning is detached eddy simulation (DES), although this is not used as frequently. In this section, these methods are briefly discussed, and their strengths and weaknesses are identified.

3.2.1 DNS - Direct numerical simulation

In the direct numerical simulation, the governing equations are solved numerically without using any turbulence models. This means that all spatial and temporal scales of turbulence must be resolved. As a result, this method is unrivalled in terms of accuracy and level of description. Although this method appears as the most obvious choice for simulating turbulent flows, unfortunately, it contains some restrictions.

For instance, all the spatial length scales must be resolved in the computational mesh. This includes the small Kolmogorov scales, η_k, up to the integral scale, L. This is only achievable when

$$L \leq N\Delta x \text{ and } \Delta x \leq \eta_k \tag{3.11}$$

where N is the number of grid points in each direction and Δx is the grid spacing. The relation between turbulent Reynolds number and turbulent length scales could be expressed as

$$Re_t^{3/4} = \frac{L}{\eta_k} \tag{3.12}$$

which means that the number of grid points required in DNS simulations must satisfy $N > Re_t^{3/4}$ [31]. In addition, considering that the time step, Δt, must be small enough to capture the fluid movement within a fraction of the grid spacing, it is evident that the

DNS method is very computational demanding. Even with low Reynolds numbers, the computational cost exceeds the benefit of the accuracy. As a consequence, the DNS method is not applicable for industrial purposes, but is considered to be a useful tool in the research of turbulence [32, 33].

3.2.2 Large eddy simulation

In LES, the large-scale eddies are resolved by using the filtered form of the governing equations, while the small-scale eddies are resolved by models. This is the result of Kolmogorov's theory of self-similarity, where the large eddies are dependent on the geometry, while the small eddies are considered to be universal [34]. Mathematically, this is achieved by spatial filtering. The filtering of the flow variable ϕ is defined as

$$\tilde{\phi}(x,t) = \int G[(x-x');\Delta]\phi(t,x')dx' \tag{3.13}$$

where G is the filtering function and Δ is the filter width. Generally, the LES filtering is obtained by using an implicit approach, where the scale of the filtered eddies is determined by the computational grid itself. The result of the filtering is velocity field variables that are divided into a resolved part, $\bar{\phi}$, and a subgrid part, ϕ',

$$\phi(x,t) = \bar{\phi}(x,t) + \phi'(x,t) \tag{3.14}$$

where ϕ denotes the pressure, energy, or velocity components. In the new set of governing equations, additional terms are required to close the equations. This is the result of the interaction between the large, resolved eddies and the small, unresolved eddies. The effects of this interaction need to be modelled using subgrid-scale (SGS) models [35–37].

The LES method is considered to be an intermediate tool between DNS and RANS. It provides results with less accuracy compared to DNS, but the computational cost is exceedingly decreased. Compared to the RANS method, LES is more accurate but comes with higher computational demand. As mentioned in chapter 1, the recent advances in computer power have increased the usage of the LES method for engineering purposes [38, 39].

3.2.3 Reynolds Averaged Navier Stokes

In the RANS method, an instantaneous flow variable is decomposed into a mean part and a fluctuating part, as shown in Eq.(3.15)

$$\phi(x,t) = \bar{\phi}(x,t) + \phi'(x,t) \tag{3.15}$$

In this equation, $\bar{\phi}$ and ϕ' denotes the averaged part and the fluctuating part, respectively. Because of non-linearity, the decomposition of the governing equations introduces additional unknown terms. To illustrate this, the equation of mass conservation is decomposed into,

$$\frac{\partial \bar{\rho}}{\partial t} + \frac{\partial}{\partial x_i}\left(\overline{\rho u_i} + \overline{\rho' u_i'}\right) = 0, \tag{3.16}$$

where the bar represents the averaging in either space or time, depending on the characteristics of the flow. The additional term $(\overline{\rho' u_i'})$, represents the interaction between density and velocity fluctuations and is a result of the decomposition. Additional models have to be applied to close this term.

Favre averaging could be used instead, to eliminate the interaction of density fluctuations. In Favre averaging, ϕ is decomposed as

$$\phi(x,t) = \tilde{\phi}(x,t) + \phi''(x,t), \tag{3.17}$$

where $\tilde{\phi}$ denotes the mean value, while ϕ'' represents the fluctuating part. Favre averaging also includes additional terms, but the correlation between density and velocity fluctuations are discarded, which is useful for flows where the density differs. The new, unknown terms need to be modelled to close the governing equations [40, 41].

The RANS method is the most commonly used approach in CFD. This is because the RANS method is less computationally demanding, compared to the DNS and LES method. The results are usually represented with adequate accuracy, which makes this method applicable for most engineering purposes. This becomes more evident when the simulations are increasingly demanding.

3.2.4 Detached eddy simulation

Detached eddy simulation (DES) is a hybrid approach between LES and RANS. The motivation for this model is the complications of the LES method in near-wall regions and the passive development of RANS models. The DES method attempts to use RANS for near-wall

regions, and LES for the rest of the flow if the grid is fine enough. Thus, combining the best features of both [42].

The first version of this method used the Spalart-Allmaras RANS model [43], where the distance, d, is replaced by

$$\tilde{d} = min(d, C_{DES}\Delta), \tag{3.18}$$

where C_{DES} is a constant, and Δ is the largest grid spacing in all three directions. The result of this is that the model acts as a RANS model when $d << \Delta$, and as a SGS model when $\Delta << d$.

The DES method could be used in many different simulations, and, in theory, be combined with any RANS model containing an appropriately defined length scale *(d)* [44]. By combining the LES and RANS method, the results are more accurate than standard RANS models, while being less computational demanding compared to LES.

3.3 Turbulent flow modelling

3.3.1 Favre filtered governing equations

The governing equations in section (3.1) are just general formulations, and not modified in order to solve the equations. As mentioned, it is necessary to apply some form of averaging or filtering to close the equations. To account for the density fluctuations associated with compressible flows, Favre-averaging is applied to the equations in section (3.1). The governing equations are then expressed as

$$\frac{\partial \bar{\rho}}{\partial t} + \frac{\partial}{\partial x_i}(\bar{\rho}\tilde{u}_i) = 0 \tag{3.19}$$

$$\frac{\partial}{\partial t}(\bar{\rho}\widetilde{u_i}) + \frac{\partial}{\partial x_j}(\bar{\rho}\widetilde{u_i}\widetilde{u_j}) + \frac{\partial \bar{p}}{\partial x_i} = \frac{\partial}{\partial x_j}(\widetilde{\tau_{ij}} + \tau_{ij}^T) \tag{3.20}$$

$$\frac{\partial}{\partial t}(\bar{\rho}\widetilde{E}) + \frac{\partial}{\partial x_i}(\bar{\rho}\widetilde{u_i}\widetilde{E}) + \frac{\partial}{\partial x_i}(\widetilde{u_i}\bar{p}) = -\frac{\partial}{\partial x_i}(\widetilde{q_i} + q_i^T) + \frac{\partial}{\partial x_j}\widetilde{u_i}(\widetilde{\tau_{ij}} + \tau_{ij}^T). \tag{3.21}$$

The $\bar{(\cdot)}$ operator represents a Reynolds operator (time-average), while the $\tilde{(\cdot)}$ denotes the density weighted flow variables. The variables, ρ, u, p and E represents the density, velocity, pressure and the total energy of a fluid, respectively. The term $\widetilde{\tau_{ij}}$ is the shear stress tensor, and is expressed by

$$\widetilde{\tau_{ij}} = 2\mu\widetilde{S_{ij}} - \frac{2}{3}\mu\delta_{ij}\widetilde{S_{kk}} \tag{3.22}$$

where μ is the dynamic viscosity, and δ_{ij} is the Kronecker delta. $\widetilde{S_{ij}}$ is the rate of strain tensor, and is written as

$$\widetilde{S_{ij}} = \frac{1}{2}\left(\frac{\partial \widetilde{u_i}}{\partial x_j} + \frac{\partial \widetilde{u_j}}{\partial x_i}\right). \tag{3.23}$$

The heat flux, $\widetilde{q_i}$, is expressed by Fourier's law of conduction [30]

$$\widetilde{q_i} = -C_p \frac{\mu}{Pr}\frac{\partial \widetilde{T}}{\partial x_i}, \tag{3.24}$$

where C_p is the specific heat capacity, T is the temperature and Pr is the dimensionless Prandtl number. The expression for the turbulent stress tensor τ_{ij}^T, and the turbulent heat flux q_i^T, bear some resemblance to Eq. (3.3) and Eq. (3.9), but do have some decisive differences.

$$\tau_{ij}^T = -\overline{\rho u_i'' u_j''} = 2\mu_t \widetilde{S_{ij}} - \frac{2}{3}\bar{\rho} k \delta_{ij} \tag{3.25}$$

$$q_j^T = C_p \overline{\rho u_j'' T} = -C_p \frac{\mu_t}{\mathrm{Pr}_t}\frac{\partial \widetilde{T}}{\partial x_j} \tag{3.26}$$

Two of the most paramount discrepancies is the inclusion of the turbulent viscosity μ_t, and the turbulent Prandtl number Pr_t. The turbulent viscosity is estimated using turbulence models, while the turbulent Prandtl number is usually assumed to be constant [45]. Another notable difference between Eq. (3.3) and Eq. (3.27) is the last term, where k represents turbulent kinetic energy, which might be a subject for further modelling depending on the selected turbulence model.

3.3.2 Turbulence modelling

In RANS methodology, it is crucial to employ turbulence models to anticipate the turbulent flow pattern, and several different models have been developed to provide accurate approximations of the turbulent flow. The $k-\varepsilon$ model [46] and the $k-\omega$ model [47] are two of the most popular turbulence models in CFD. Incidentally, both the aforementioned models have some limitations when applied to CHT simulations in turbomachinery. The $k-\varepsilon$ model is inadequate for separated flows (e.g. airfoils), while the $k-\omega$ model is very sensitive to inlet- and free-stream boundaries [48].

To address these issues, Menter [49] developed the shear stress transport (SST) $k-\omega$ model. The model adds an additional cross-diffusion term, which contains the scalar product of the turbulent kinetic energy k, and the specific dissipation rate ω, and a blending function that incorporates the cross-diffusion term far from the walls, but not near the walls. The result

of this is that the model behaves as $k-\varepsilon$ in the free-stream, and as $k-\omega$ near the walls, thus combining the best features of both. As a consequence, the SST $k-\omega$ model is frequently used in simulations containing flow-separation and large pressure gradients. Zheng et al. [50] compared the commercially available turbulence models against the experimental results by Hylton et al. [11], and the conclusion presented the $SSTk-\omega$ turbulence model as the most accurate, hence the selected model for this study.

The turbulent viscosity μ_t is calculated from

$$\mu_t = \rho k T_t, \tag{3.27}$$

where k is the turbulent kinetic energy and T_t represents the turbulent time scale which is expressed as

$$T_t = min\left(\frac{\alpha^*}{\omega}, \frac{a_1}{SF_2}\right). \tag{3.28}$$

ω denotes the specific dissipation rate, S is given by Eq.(3.4), and both α^* and a_1 are model coefficients. F_2 is a blending function which is calculated as

$$F_2 = tanh\left(\left(max\left(\frac{2\sqrt{k}}{\beta^*\omega d}, \frac{500\nu}{d^2\omega}\right)\right)^2\right) \tag{3.29}$$

where β^* is a coefficient, d is the wall distance and ν is the kinematic viscosity. The transport equations for the turbulent kinetic energy k, and the specific dissipation rate ω are

$$\frac{\partial}{\partial t}(\rho k) + \frac{\partial}{\partial x_i}(\rho k u_i) = P_k - \rho\beta^* k\omega + \frac{\partial}{\partial x_i}\left[(\mu + \sigma_k\mu_t)\frac{\partial k}{\partial x_i}\right] \tag{3.30}$$

$$\frac{\partial}{\partial t}(\rho \omega) + \frac{\partial}{\partial x_i}(\rho \omega u_i) = P_\omega - \rho\beta\omega^2 + \frac{\partial}{\partial x_i}\left[(\mu + \sigma_\omega\mu_t)\frac{\partial \omega}{\partial x_i}\right]. \tag{3.31}$$

β^*, β, σ_k and σ_ω are model coefficients, while the two production terms, P_k and P_ω are expressed as

$$P_k = min\left(\tau_{ij}\frac{\partial u_i}{\partial x_j}, 10\beta^*\rho k\omega\right) \tag{3.32}$$

$$P_\omega = \gamma\rho S^2 + 2\rho(1-F_1)\frac{\rho\sigma_{\omega 2}}{\omega}\frac{\partial k}{\partial x_j}\frac{\partial \omega}{\partial x_j}. \tag{3.33}$$

Eq.(3.32) and Eq.(3.33) contains the additional coefficients γ and $\sigma_{\omega 2}$. The term F_1 is another blending function defined as

$$F_1 = tanh\left(\left[min\left(max\left(\frac{\sqrt{k}}{0.09\omega d}, \frac{500\nu}{d^2\omega}\right), \frac{2k}{d^2 CD_{k\omega}}\right)\right]^4\right), \tag{3.34}$$

where $CD_{k\omega}$ represents the cross-diffusion coefficient. All the coefficients and their formulations as summarised in table 3.1.

Table 3.1 Model coefficients [51]

a_1	0.31	σ_k	$F_1\sigma_{k1}$+(1-F_1)σ_{k2}
α^*	$F_1\alpha_1^*$+(1-F_1)α_2^*	σ_{k1}	0.85
α_1^*	1	σ_{k2}	1
α_2^*	1	σ_ω	$F_1\sigma_{\omega 1}$+(1-F_1)$\sigma_{\omega 2}$
β^*	$F_1\beta_1^*$+(1-F_1)β_2^*	$\sigma_{\omega 1}$	0.5
β_1^*	0.09	$\sigma_{\omega 2}$	0.856
β_2^*	0.09	γ	$F_1\gamma_1$+(1-F_1)γ_2
β	$F_1\beta_1$+(1-F_1)β_2	γ_1	$\frac{\beta_1}{\beta^*}$ - $\sigma_{\omega 1}\frac{k^2}{\sqrt{\beta^*}}$
β_1	0.075	γ_2	$\frac{\beta_2}{\beta^*}$ - $\sigma_{\omega 2}\frac{k^2}{\sqrt{\beta^*}}$
β_2	0.0828	-	-

Chapter 4

Experimental and numerical details

4.1 Experimental details

In this study, one of the two aerothermodynamic investigations presented by Hylton et al. [11] is used to validate the numerical model. The objectives of the original report were to acquire experimental data to verify the results of a 2D heat transfer modelling technique. In the original experiments, three C3X turbine guide vanes are located in a free-stream. The centre vane is subjected to evaluation, while the two adjacent slave vanes are included to ensure steady-state aerodynamic conditions. The test vane is convectively cooled by ten radial cooling passages from the hub to the shroud, where air is the cooling medium. The passages have circular cross-sections and are supplied with air from individual metered lines. The geometric configuration of the vane is adopted from the experimental report [11], where the constant cross-section is located in the x-y plane, as shown in fig. 4.1. The height of the vane is 76.2 mm, and it has no twist. It is observed that the cooling holes are arranged according to the curvature of the centreline, except the holes near the leading edge. The geometrical specifications of the vane are summarised in table 4.1.

Table 4.1 Geometric parameters of C3X vane

Setting angle (°)	59.89
Air exit angle (°)	72.38
Throat (mm)	32.92
Vane height (mm)	76.2
Vane spacing (mm)	117.73
True chord (mm)	144.93
Axial chord (mm)	78.16

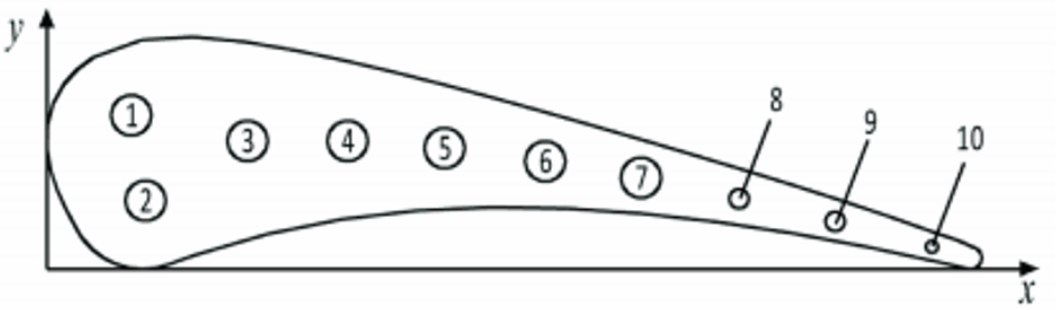

Fig. 4.1 Schematic of the NASA C3X vane with enumerated cooling channels, as reported in the original report [11].

The test section contains turbulence augmentation rods, followed by static pressure taps, which is located 187.2 mm from the leading edge of the vanes. The ensuing exit static pressure taps are located 90.2 mm from the leading edge. The walls are cooled using steam to prevent heat radiation and to keep the temperature similar to the vane surface temperature. Therefore, the walls are considered to be adiabatic. The inlet of the computational model coincides with the inlet pressure taps. The outlet is located further downstream to eliminate the effects of turbulence, while a periodic outlet is included to ensure that the physics is incorporated. Due to periodicity, the mainstream is restrained by two planes separated by 117.73 mm in the y-direction, which follows the centre-curvature of the vane. This will also reduce the computational demand of the simulations. To ensure fully developed flow and eliminate unwanted effects, such as reversed flow, both the inlet and outlet of the cooling channels are extruded 50 mm. A schematic of the computational models with boundaries is shown in fig. 4.2

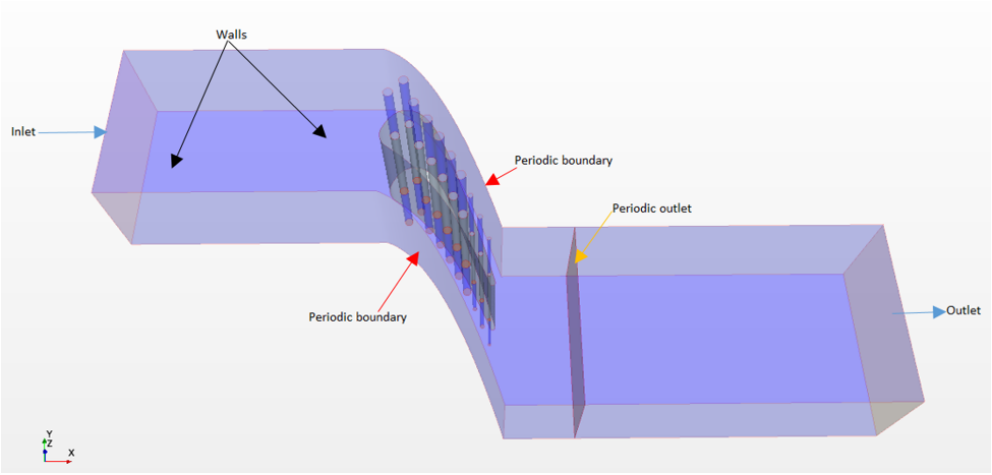

Fig. 4.2 Computational domain used in the simulations.

In the original report, the experimental data were obtained by instrumenting the test vane with approximately 80 thermocouples and 30 static pressure taps. The thermocouples were located at a plane near midspan of the vane and were placed in 0.58 mm deep radial grooves. The grooves were then covered by cement, and blended by hand to ensure a smooth surface. To minimise the errors from the grooves, the vane was made of ASTM310 type stainless steel, with a relatively low thermal conductivity. Similarly to the thermocouples, the static pressure taps were mounted near the midspan. The distribution of the pressure taps was denser near the leading edge, to adequately capture the large pressure gradients in this area. The installation of the pressure taps was performed similarly to the thermocouples. Each of the cooling channels was instrumented with thermocouples and static pressure taps at the inlet and the outlet. The temperature measurements on the vane surface were specified as a well-developed technique, with a proclaimed uncertainty of $\pm\ 1^{\circ}C$. The free-stream temperature measurements had a reported uncertainty of $\pm\ 11^{\circ}C$, due to the fluctuations from the facility combustor. As a result, the calculations of the heat transfer coefficients were severely affected by this. The pressure measurements were described with an uncertainty of $\pm\ 0.7kPa$.

It was concluded that the heat transfer and aerodynamic distributions from the experimental measurements appeared to be reasonable. The report showed that the heat transfer distribution on the suction surface of the C3X vane was highly dependent on the Reynolds number, due to the transitional nature of the flow. Consequently, the overall heat transfer level is affected by the Reynolds number. It was also proved that the Mach number distribution also influences the heat transfer level. From the analytical part of the report, it was deduced that the turbulence model and turbulent heat flux require further development. It was shown that the surface pressure predictions were unsatisfactory with the available turbulence models. Even though the analytical tools were proven to be inadequate, the report provided high-quality data sets for airfoil heat transfer, which has been important in the development of modern analytical models.

4.2 Physics models

The computational tool used in this study is the commercial software STAR CCM+. The first part of setting up the simulation is to select physics models. The physics models defines the physical phenomenon in a continuum, along with the primary variables of the simulation. In addition, the mathematical formulations used to generate a solution is prescribed to the different continuums. It is necessary to select the right combination of models to successfully define a physics continuum. The selected physics models for the two fluids and the vane are summarised in table 4.2 and 4.3, respectively.

Table 4.2 Selected physics models for the hot and cold fluids

Model parameter	Selected model
Space	Three dimensional
Time	Steady
Material	Gas
Flow	Coupled flow
Equation of state	Ideal gas
Energy	Coupled energy
Viscous regime	Turbulent
Reynolds-Averaged turbulence	SST k-ω
Wall treatment	All-y^+ wall treatment
Optional	Cell quality remediation
Optional	Solution interpolation

Table 4.3 Selected physics models for the C3X vane

Model parameter	Selected model
Space	Three dimensional
Time	Steady
Material	Solid
Energy	Coupled solid energy
Equation of state	Constant density
Optional	Cell quality remediation
Optional	Solution interpolation

Some of the models are selected for obvious reasons, while others require some justifications. Although most flows are transient, particularly when heat transfer is involved, the time model is set to be steady. For heat transfer simulations involving both fluids and solids, the physical response time is very different. The flow reaches thermal stability very

quickly, while the solid requires much more time. When modelling time as steady, the concept of time is meaningless, and the simulations reach convergence faster. The coupled flow model is selected because of the ability to handle compressible flows. The coupled energy model is an extension of the coupled flow model, where the governing equations are solved simultaneously. This model is also very important for conjugated heat transfer.

The all-y^+ wall treatment model is a hybrid, which combines the features of the high y^+ wall treatment for coarser meshes, and the low y^+ wall treatment for finer meshes. This is useful for simulations with varying mesh density. The importance of the dimensionless distance y^+ is further discussed in section 4.5. The two optional models, cell quality remediation and solution interpolation were selected to ensure numerical stability and convergence. Cell quality remediation identifies cells with inadequate quality and modifies them to improve the robustness of the solution. The solution interpolation model is used when re-meshing occurs, where the original results are interpolated onto a new mesh. This is effective for finding the appropriate mesh for the simulation. The remaining models are further discussed in the following sections.

4.3 Initial conditions

The initial conditions of a simulation serve as a starting solution and are only enforced at the beginning of the simulation. For cases involving temperature, it is preferable to set the initial conditions close to the expected results. This will help the simulation converge and save computational time. The most important initial conditions used in this study are summarised in table 4.4, while the remaining parameters are set as default values provided by the software.

Table 4.4 Initial conditions of the regions

Continuum	Static temperature (K)	Pressure (Pa)
Coolant	320	101325
Hot gas	700	320000
C3X Vane	550	-

4.4 Boundary conditions

To validate the numerical model, the boundary conditions imposed on the external gas stream and the internal cooling channels are set according to code 4521, run no. 157 from the original experiments [11]. The inlet of the external gas stream is defined as a stagnation inlet to assign the boundary with uniform total pressure (P_{Tin}), and total temperature (T_{Tin}) conditions. Both outlets of the gas stream and all the outlets of the cooling channels are defined as pressure outlets to impose static pressure (P_{Sout}) conditions at these boundaries. The inlets of each cooling channel are prescribed as mass flow inlet, with a fixed mass flow rate ($\dot{M}_{in}$) and constant static temperature (T_C) specified at each boundary. In addition, the turbulence intensity (T_u) and viscosity ratio (T_v) are fixed at the inlet of the external gas stream, while turbulence intensity (T_u) and hydraulic diameter (D_h) are specified at the inlet of each cooling channel. All the details of the boundary conditions are given in tables 4.5 and 4.6, respectively.

Table 4.5 Boundary conditions of the external gas stream

P_{Tin} (Pa)	T_{Tin} (K)	P_{Sout} (Pa)	T_u (%)	T_v
413286	818	254172	8.3	30

Table 4.6 Boundary conditions of the cooling channels used for both air and steam

Channel number	$\dot{M}_{in}$ (g/s)	T_C (K) [50, 52]	D_h (mm)	T_u (%)
1	22.2	342	6.3	10
2	22.1	344	6.3	10
3	21.8	335	6.3	10
4	22.8	336	6.3	10
5	22.5	330	6.3	10
6	22.5	355	6.3	10
7	21.6	336	6.3	10
8	7.44	350	3.1	10
9	4.77	377	3.1	10
10	2.56	387	1.98	10

The solid vane is made of ASTM type 310 stainless steel, with a relatively low thermal conductivity. The density (ρ) and the specific heat capacity (C_P) is reported as constant over the range of temperatures applicable for this study [53]. The values are set as 8030 kg/m^3 and 502 $J/kg \cdot K$, respectively. The thermal conductivity is assumed to vary linearly with

temperature and is expressed as

$$k_s = 0.0115 \cdot T + 9.9105 (W/m \cdot K). \tag{4.1}$$

Both the external hot gas and the cooling mediums is assumed to be operating under ideal gas conditions. Sutherland's formula is used to describe the temperature dependent dynamic viscosity (μ) and thermal conductivity (k_g), which are given by

$$\mu(T) = \mu_0 \left(\frac{T}{T_0} \right)^{3/2} \cdot \frac{T_0 + M}{T + M}, \tag{4.2}$$

$$k_g(T) = \lambda_0 \left(\frac{T}{T_0} \right)^{3/2} \cdot \frac{T_0 + S}{T + S}, \tag{4.3}$$

where the constants are represented in table 4.7.

Table 4.7 Sutherland constants for air and steam [54]

Constant	Air	Steam
μ_0 (Pa·S)	$1.7894 \cdot 10^{-5}$	$1.12 \cdot 10^{-5}$
T_0 (K)	273.11	350
M (K)	110.56	1064
λ_0 (W/m·K)	0.0216	0.0181
S (K)	194	220

The specific heat capacity (C_p) of both cooling mediums is described by a polynomial temperature dependence, which is expressed as

$$C_p = a_0 + a_1 T + a_2 T^2 + a_3 T^3 + a_4 T^4, \tag{4.4}$$

where the constants are given in table 4.8.

Table 4.8 Constants for polynomial specific heat capacity [55]

Constant	Air	Steam
a_0	957.110256	1563.077
a_1	0.2365234	1.603755
a_2	$5.141114 \cdot 10^{-6}$	-0.002932784
a_3	$-3.3917446 \cdot 10^{-9}$	$3.216101 \cdot 10^{-6}$
a_4	$-6.0929646 \cdot 10^{-12}$	$-1.156827 \cdot 10^{-9}$

4.5 Computational mesh

In this study, an unstructured mesh is generated in the fluid domain, the cooling channels and in the turbine guide vane. At first, a polygonal surface grid is generated on the different 2D planes, which is then stretched across the volume to create the different domains for the simulations. The outcome of this operation is a volume mesh consisting of polyhedral elements. Compared to a tetrahedral mesh, a polyhedral mesh requires about four times fewer cells for the same base size and is more numerically stable, thus reducing the computational cost of the simulations [56]. In addition, the generation of conformal grids is easier for polyhedral elements, relative to hexahedral elements. The importance of conformal grids is particularly essential for CHT simulations, where information is exchanged between boundaries. Fig. 4.3 is included to better illustrate the difference between a conformal and a non-conformal mesh. As depicted, the cells in the different regions are aligned when the mesh is conformal. This is shown by the smooth transition from a cooling channel to the vane. On the other hand, the cells in the non-conformal mesh are not aligned. As a consequence, information is not as easily passed between the boundaries, which might cause the simulation to diverge.

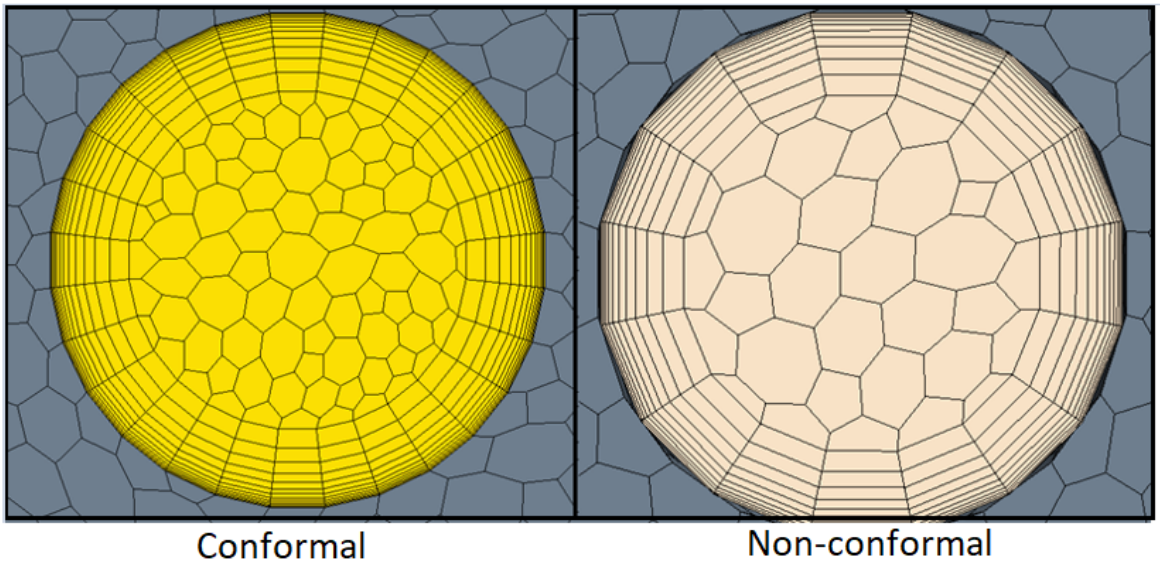

Fig. 4.3 Depiction of a conformal (left) and non-conformal mesh (right).

The meshers selected in this study is the surface remesher, automatic surface repair, polyhedral mesher and prism layer mesher. In addition, the mesh generator is set to run three optimisation cycles to further enhance the quality. The settings used to generate the final mesh is shown in table 4.9.

Table 4.9 Global mesh settings

Parameter	Value
Base size	12 cm
Base size (Channel 1-7)	8% (Relative to base)
Base size (Channel 8 & 9)	4% (Relative to base)
Base size (Channel 10)	2% (Relative to base)
Target surface size	100% (Relative to base)
Minimum surface size	5% (Relative to base)
Surface curvature	48 Pts/circle
Surface growth rate	1.1
Volume growth rate	1.2

To fully resolve the near-wall flow behaviour, the cells adjacent to the solid boundaries need to be fine enough to capture the boundary layer of the flow. For this reason, prism layers are generated near the fluid/solid boundaries of the mesh. The total height of the prism layer should be equal, or higher than the boundary layer. To determine the height of the prism layers, the dimensionless wall distance y^+ is introduced. This parameter is expressed as

$$y^+ = \frac{yu_\tau}{\nu}, \tag{4.5}$$

where y is the absolute distance from the wall, u_τ is the friction velocity and ν is the kinematic viscosity. To fully resolve the boundary layer, the height of the first cell should be within the viscous sublayer, where $y^+ < 5$ [57, 58]. A schematic of the mesh used in this study is shown in fig. 4.4, where a detailed representation of the prism layers near the boundaries is included. To save computational resources, prism layers were not applied on the adiabatic walls and periodic planes. For the same reason, the extruded regions of the free-stream and the cooling channels consists of hexahedral elements. The details surrounding the prism layers are summarised in table. 4.10.

Table 4.10 Prism layer settings for the cooling channels and the vane external surface

Parameter	Cooling channels	Vane external surface
Number of prism layers	12	15
Prism layer stretching	1.3	1.25
Prism layer total thickness (cm)	0.1	0.1

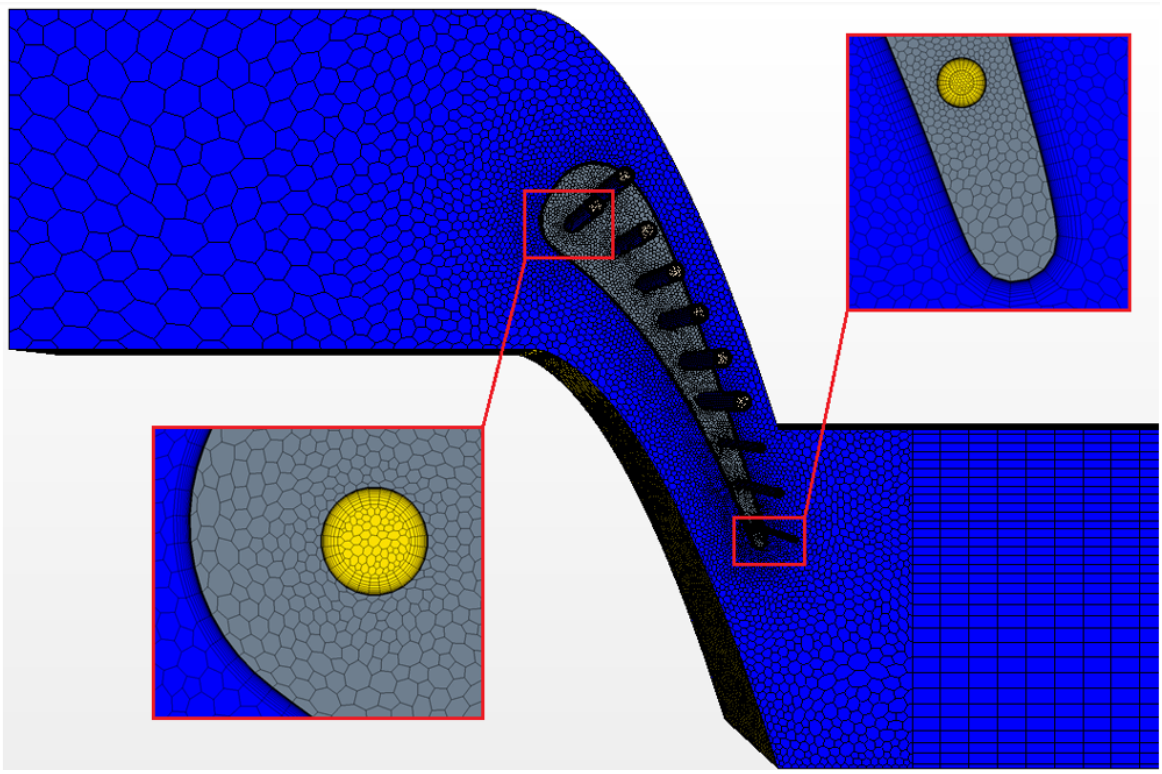

Fig. 4.4 Schematic of the generated mesh in the X-Y plane, with detailed representation of the leading and trailing edge of the vane.

4.6 Hardware

Running CFD simulations on a computer might be very computational demanding. This implies that the simulations demand much from the processor (CPU) and the temporary memory (RAM). One of the most influential aspects is the number of cells in the mesh. It is proclaimed that the STAR-CCM+ software requires at least 1GB of RAM per million cell [59], which demonstrates the importance of sufficient computer hardware. In this study, the simulations were executed with the specifications listed in table 4.11.

Table 4.11 Hardware specifications of the computer

Hardware	Specification
CPU	Intel(R) Core(TM) i7-6700 CPU @ 3.40GHz
RAM	16 GB DDR4-2400 non-ECC SDRAM

4.7 Mesh independence

To determine if the mesh is sufficient, a mesh independence test is performed. The motivation for this test is to show that the mesh resolution has no influence on the results from the simulations. The results from the mesh independence test is presented in fig. 4.5

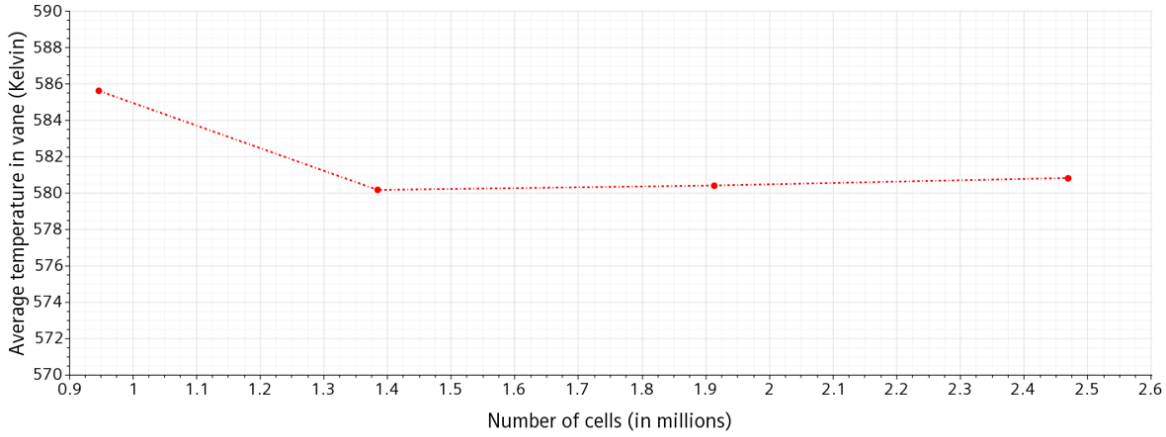

Fig. 4.5 Mesh independence test.

As shown in fig. 4.5, six different mesh densities are tested under the same conditions. The parameter used for comparison is the volume average temperature that arises in the vane. The results show that mesh independence is achieved at approximately 1.4 million cells. In fact, the difference between the results is less than 0.5% after this point. To save computational resources, while keeping a decisive accuracy, the mesh containing 1.9 million cells is selected for further investigations, which is shown in fig. 4.4.

4.8 Convergence

To evaluate if the simulation has reached convergence, it is necessary to assess the residuals. The residuals measure the difference between successive iterations for some of the variables in the governing equations. Fig. 4.6 represents the residual monitor plot from one of the simulations in this study. It is observed that the solution display converged behaviour and that the fluctuations are relatively small.

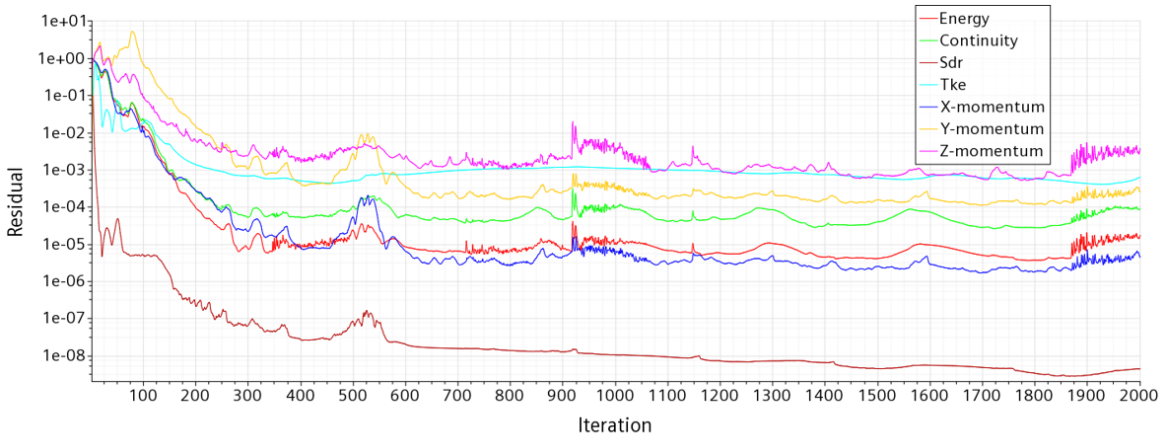

Fig. 4.6 Residuals monitor plot.

However, the residual monitors are unreliable as the sole measure of convergence. Consequently, it is important to measure relevant physical properties from the simulation to decide if the solution is converged. For this study, the volume average temperature in the vane is selected for this purpose, which is displayed in fig. 4.7. From this figure, it is deduced that simulation is converged after 2000 iterations and that the fluctuations are insignificant.

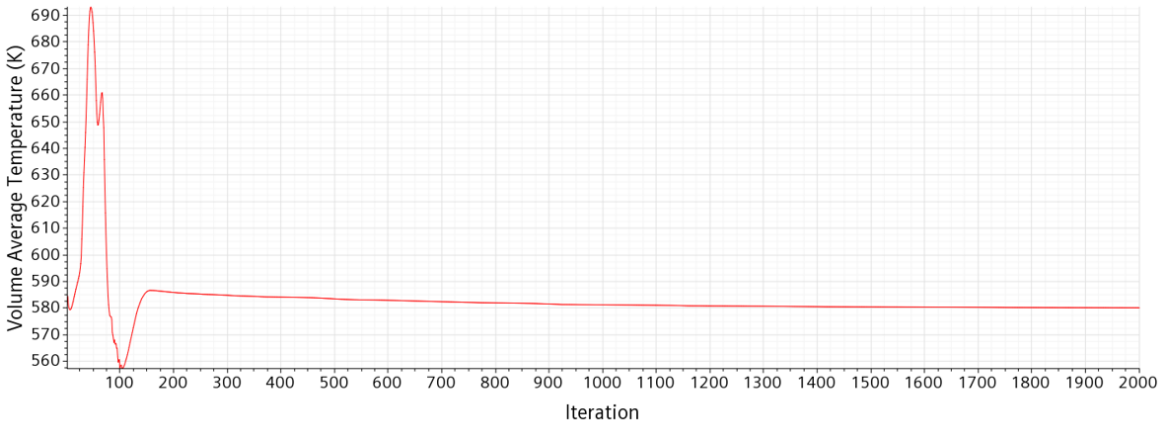

Fig. 4.7 Volume average temperature plot.

Chapter 5

Results and discussion

5.1 Model validation

5.1.1 Aerodynamic characteristics

To evaluate if the results produced by the computational model is legitimate, a comparison against the experimental results by Hylton et al. [11] is required. The dimensionless location X/L is used to show the position on the external wall of the vane. It is derived from the x-coordinate of the data points (X) and the axial chord length (L). The dimensionless location is also used to differentiate the pressure side (PS) and the suction side (SS) of the vane. The leading edge and the trailing edge is represented by $X/L = 0$ and $X/L = 1$ or -1, respectively. The pressure and temperature distribution is normalised by P/P_{ref} and T/T_{ref}, using the references values reported in [11].

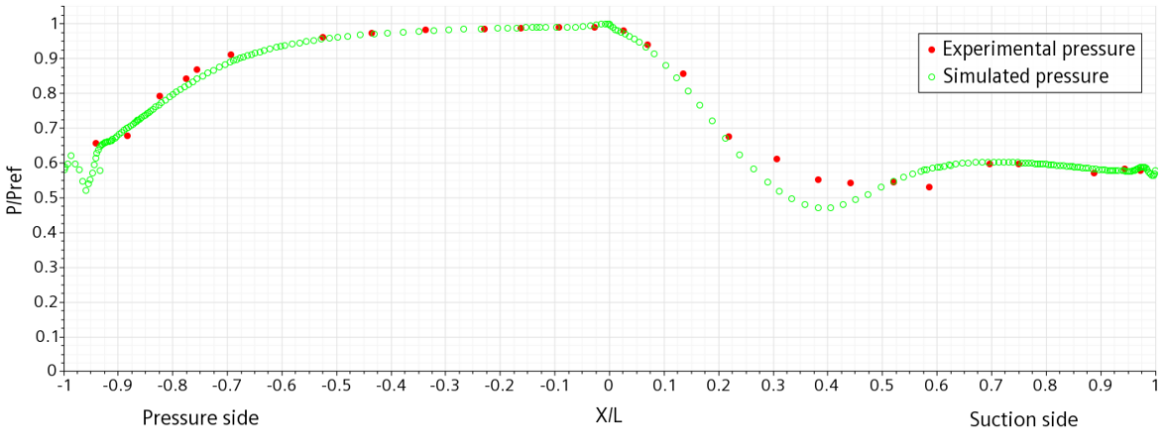

Fig. 5.1 Comparison of the normalised static pressure from the experimental report and the numerical simulations at mid-span. The reference pressure is 413286 Pa.

The static pressure distribution at mid-span is used to compare the aerodynamic characteristics of the vane. From fig. 5.1, it is observed that the numerical results on the pressure side are in very good agreement with the experimental results. On the pressure side, it is observed that the pressure declines slowly until X/L = -0.5, and then it drops drastically. When the flow is approaching the trailing edge (X/L = -1), the static pressure begins to fluctuate. On the suction side, the more complex flow behaviour leads to discrepancies between the experimental- and numerical results. From the leading edge, the flow is accelerated on the suction side. In the region where X/L is between 0.3 and 0.7, the numerical model over-predicts the acceleration. This anomaly could be explained by the turbulence model ability to consider all the complex flow phenomenon, particularly for flows with strong acceleration. However, the numerical results are still in overall good agreement with the experimental results, with an average error of 1.39%.

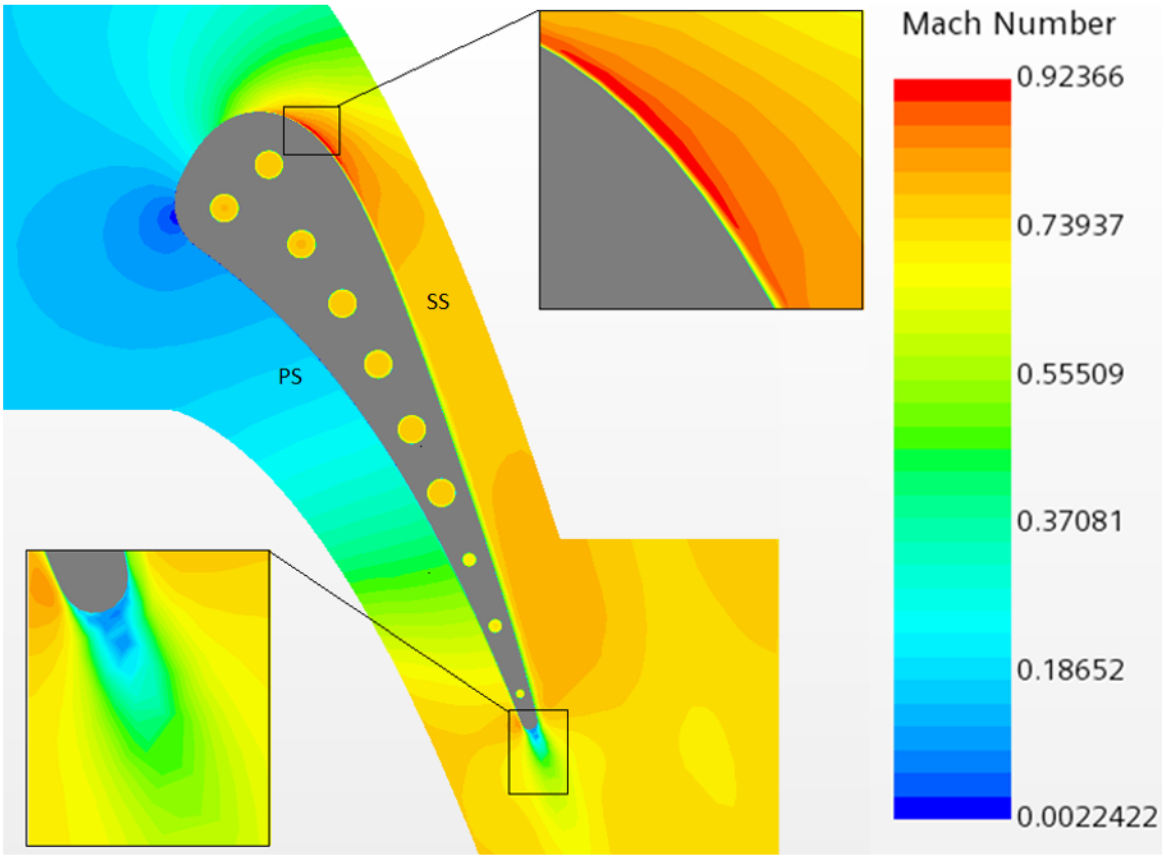

Fig. 5.2 Contours of the Mach number on the mid-span plane, including enlarged views of the transition regions on the suction side and near the trailing edge.

In order to obtain a better understanding of the discrepancies, a figure displaying the contours of the Mach number at the mid-span plane is presented in fig. 5.2. It is observed

that a stagnation point is formed near the leading edge, and the flow is split. The flow is then accelerated on both sides of the vane. On the pressure side, the Mach number increases gradually toward the trailing edge, causing the static pressure to decrease. The flow is then reunited as it passes the trailing edge, causing a reduction of the Mach number.

On the suction side, the flow accelerates rapidly toward the throat, and just after the "top" of the vane, the section containing the highest Mach numbers appears. The heat transfer is dependent on the local velocity, which is high in this area. In addition, the boundary layer in this region decreases, thus reducing the resistance to heat transfer. Coincidentally, this region corresponds with the deviations observed in fig. 5.4. After the high Mach number region, the flow is transitioning before separating near the trailing edge.

As previously mentioned, the discrepancies on the suction side are connected the numerical model. Specifically, the turbulence model. The shortcomings of the turbulence model arise in stagnation regions and regions with steep acceleration [60, 61], both present in this study. The model tends to overpredict turbulence levels in these regions, but still performs better compared to other turbulence models [50].

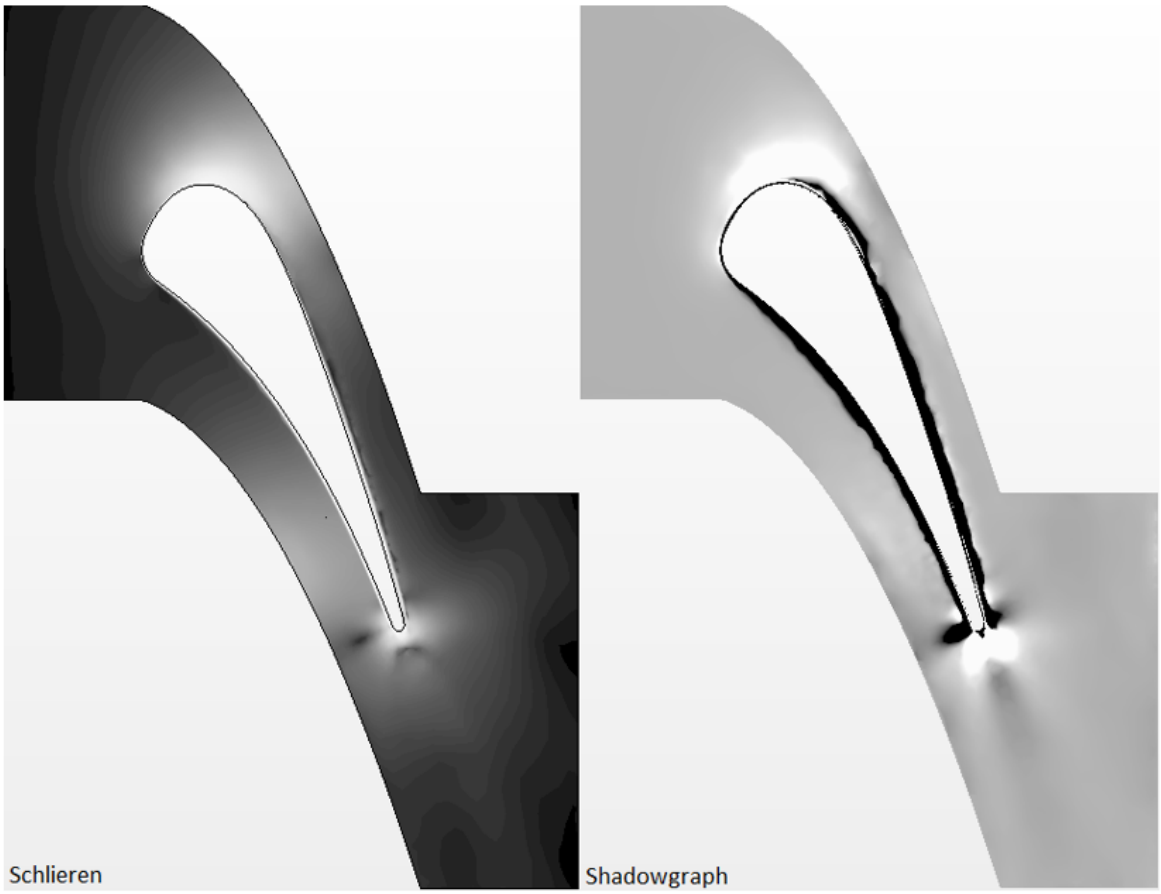

Fig. 5.3 Numerical Schlieren and shadowgraph image of the flow over the C3X vane.

To better illustrate the regions causing the discrepancies, a numerical Schlieren and a shadowgraph image is included in fig 5.3. Experimental Schlieren and shadowgraph techniques are frequently used in aerodynamics to study shock waves. The technique is based on refraction, which occurs when a wave crosses from one medium with a given density to another. When a wave encounters a change in the density of a fluid, it is bent. High Mach number regions contain large density gradients, causing light waves to bend. The phase speed difference in light is translated into changes of intensity, which is shown with light and dark regions [62]. This technique has been adopted to CFD, which makes local density fluctuations easier to identify [63]. It is the first and second derivatives of density which is used to visualise these regions in the post-processor.

The previously described high Mach regions on the C3X vane becomes much more visible in this figure. Both images clearly show two very distinct regions, one at the "top" of the vane and one after the trailing edge. Both these regions contain severe density variations, which is shown by the light and dark regions. The overpredicted turbulence causes greater density variations than expected, which affects the pressure distribution drastically. These density variations will also influence the heat transfer from the hot gas to the vane.

5.1.2 Temperature distribution

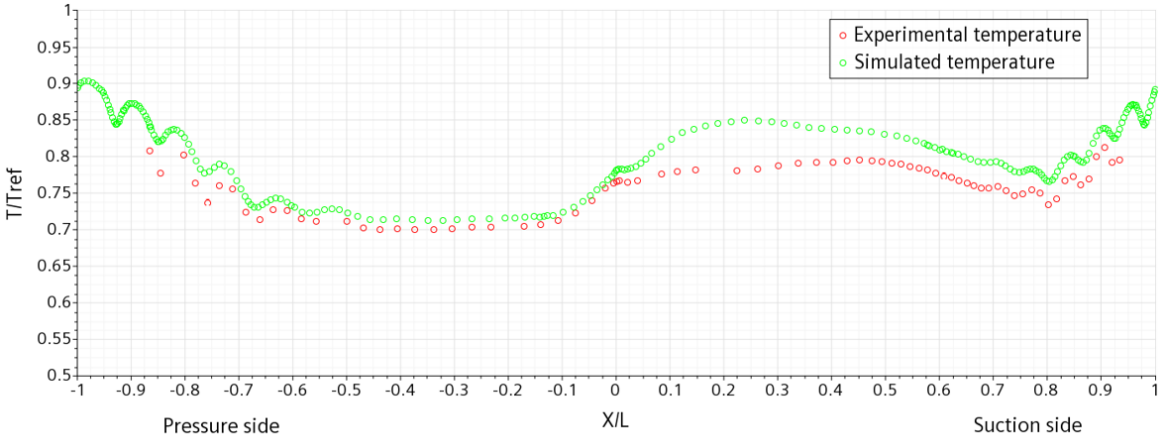

Fig. 5.4 Comparison of the normalised temperature from the experimental report and the numerical simulations at mid-span. The reference temperature is 811 K.

Fig. 5.4 shows the normalised temperature at mid-span and is used to validate the thermal effects of the flow. It is recognised that the predicted temperature on the pressure side is slightly overpredicted, but is in accordance with the experimental results. From the leading edge, the temperature is decreasing steadily until X/L = -0.5. After this point, the temperature is increasing, but is suffering from some local drops. These drops coincide with the position of the cooling channels, which are increasingly influential when the thickness of the vane is decreasing. As expected, the maximum temperature appears around the trailing edge, where the thickness is slim. Similarly to the pressure distribution, the temperature on the suction side of the vane is showing a clear distinction between the numerical results and the experiment, especially when X/L is between 0.1 and 0.6. Nevertheless, the two results are in good agreement with an average relative difference of 3.78%.

It is remarkably informative to inspect the temperature distribution across a specific cross-section, which includes all the computational regions. Such a cross-section is provided in fig. 5.5, where the temperature distribution is normalised along a specified line. As observed, the line is stretched across the domain, vane and a cooling channel (No.3). The coordinate system is based on the y-coordinates, and the dimensionless distance X indicates the distance from the centre of the cooling channel. As previously, -1 and 1 denotes the pressure and suction side, respectively. It is recognised that the temperature profile on the pressure side is different from the suction side. On the pressure side, the temperature exhibits fully developed behaviour along the inner wall of the channel, which is demonstrated by the rapid increase in temperature. This is followed by a steady increase toward the external

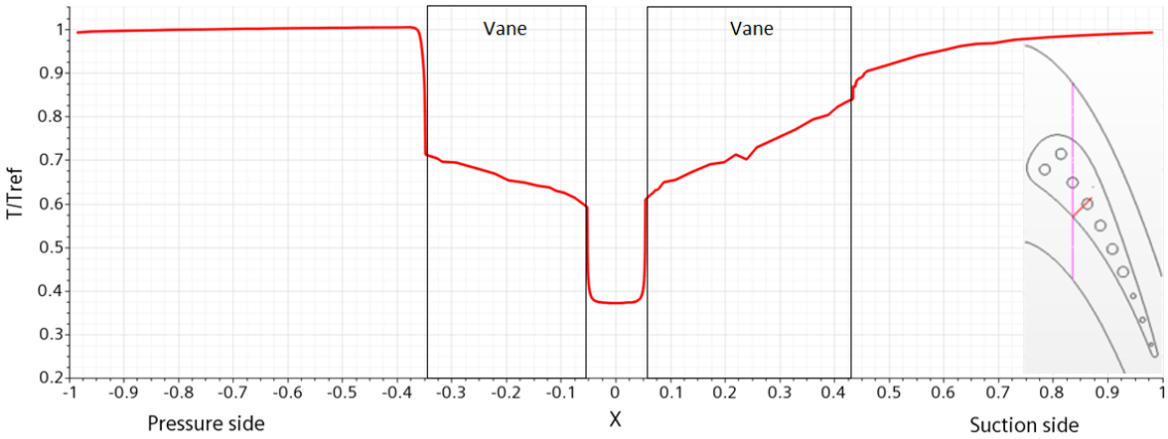

Fig. 5.5 Normalised temperature distribution along a straight line at mid-span, which cuts through all computational regions at hole number 3.

wall of the vane. The external wall features the same characteristics as the inner wall. This temperature surge implies that the thermal resistance is high, which is a result of the fully developed boundary layer.

The first part of the suction side is similar to the pressure side, where a rapid gain is followed by a steady increase through the solid vane. As opposed to the pressure side, the temperature increase adjacent to the external wall on the suction side is inferior. This is a strong indication of low thermal resistance and an incomplete transition. Incidentally, this location corresponds with the density variation regions, which has a strong effect on the temperature. In addition, it is noticed that the temperature is somewhat lower within the vane on the pressure side, compared to the suction side.

5.2 Comparison of air and steam

In this section, a comparison of numerical results between air and steam as cooling medium is presented. To better understand how the vane is affected by the cooling mediums, three different cross-sectional planes are selected to examine the disparity at different locations. These planes are located at 25%-span, mid-span and 75%-span, with the hub as the reference, shown in fig.5.6.

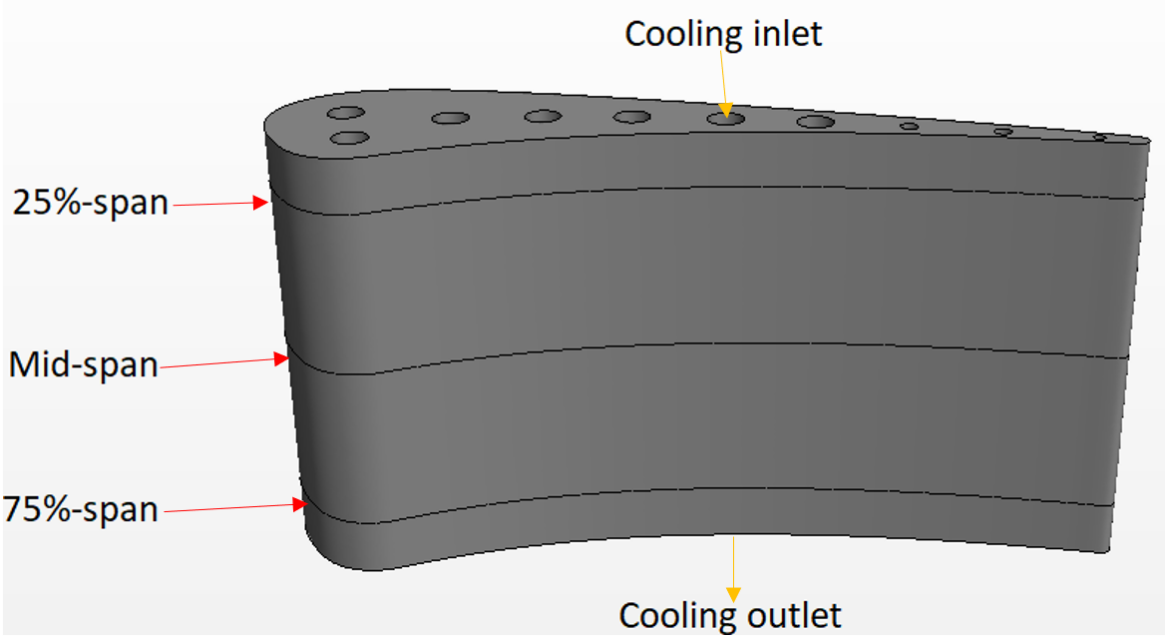

Fig. 5.6 Location of the three cross-sectional planes used for comparison.

The normalised temperature distribution at these sections are displayed in fig. 5.7, which is used to study the thermal influence on the external wall of the vane. It is observed that the temperature profiles at the different cross-sections are fairly consistent, as expected. Apart from the overall temperature, the only other noticeable difference is the fluctuations where X/L is between -1 and -0.5 on the pressure side, and between 0.7 and 1 on the suction side. In all sections, the steam results exhibit a steeper decrease and increase of temperature, and the variation between the bottom and vertex of the fluctuations are greater. This indicates that the cooling effect of steam is greater than air. In addition, it is detected that the difference between the results increases from the hub to the shroud. At first, the average difference between all data points increases from 3.89% to 4.87%, then it increases to 5.29%. The total increase is 1.6%, which is equivalent to 13 K. This implies that the temperature rise along the vane is slower when steam is used, confirming the previous statement.

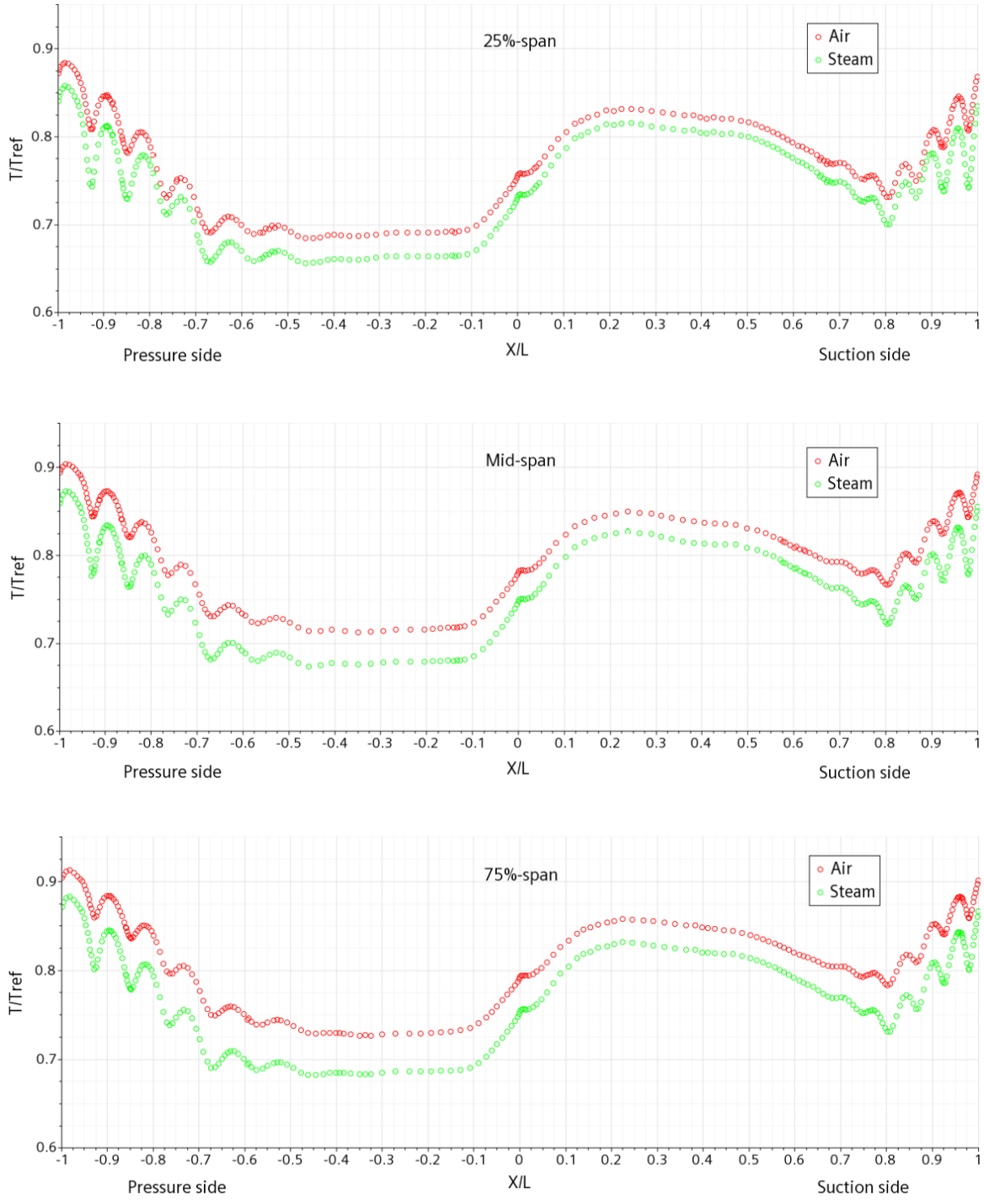

Fig. 5.7 Comparison of normalised temperature distribution at the three cross-sectional planes. The reference temperature is 811 K.

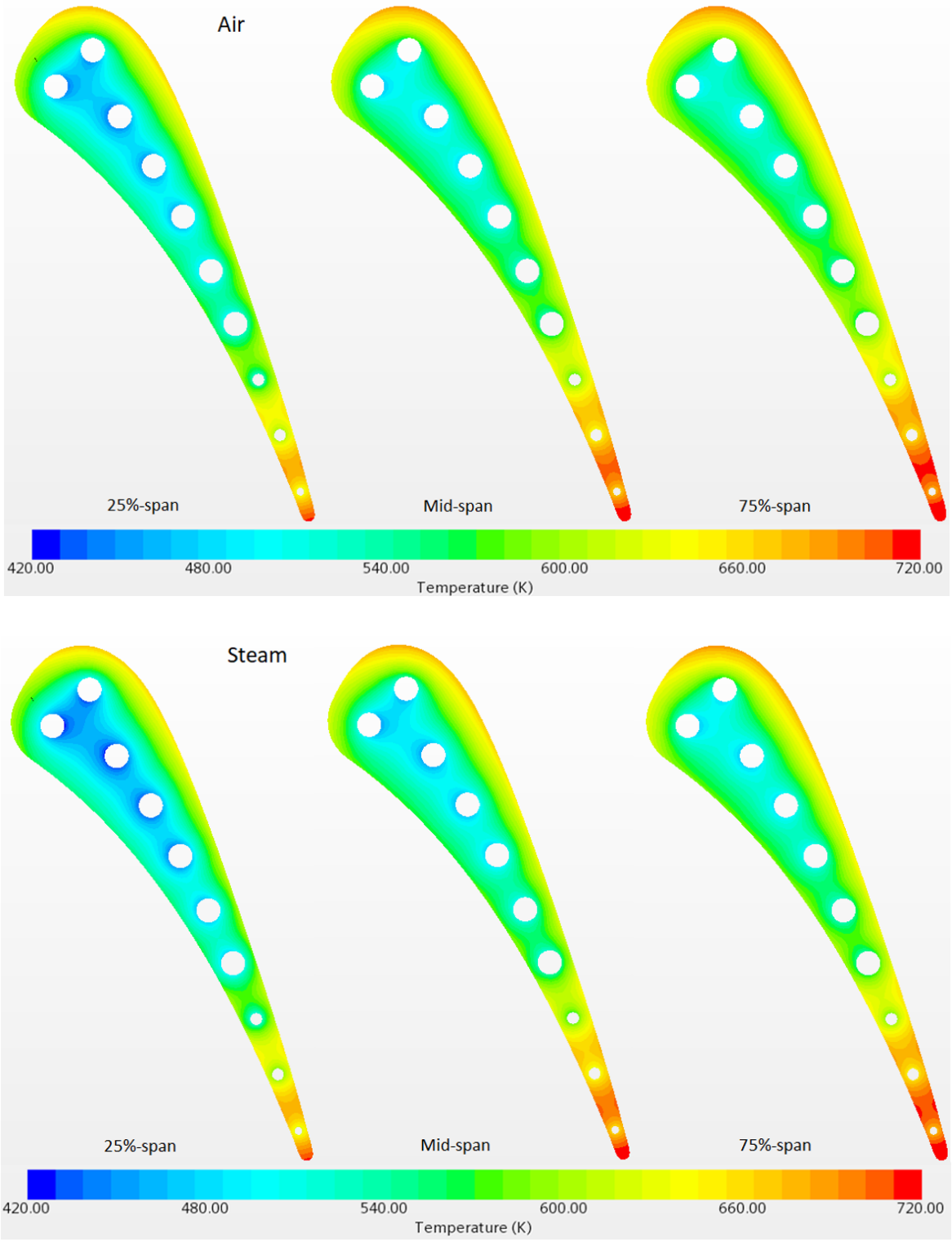

Fig. 5.8 Temperature contour comparison of the different cross-sectional planes.

Fig. 5.8 displays the temperature contours in the previously defined cross-sectional planes. It is useful to study these temperature contours to get a more complete impression of the temperature in the vane. By comparing the air and steam contours, the previously established trend is apparent. The vane gets hotter as the distance from the hub is increased, and steam is the superior cooling medium. The temperature rise in the span-wise direction is due to a decrease in the cooling effect, which is caused by an increase in the coolant temperature. Additionally, some other details are noticed from this figure. It is observed that the temperature on the pressure side is lower compared to the suction side. This is displayed by the "cooler" areas stretching toward the pressure side. Also, two areas of interest become visible in this figure. Both the "top" of the vane and the trailing edge exhibits high temperatures, suggesting that these areas are prone to high thermal loads.

The static temperature distribution on the external surface of the vane is presented in fig. 5.9. It is observed that the maximum temperature, as earlier stated, appears near the trailing edge of the vane. This is due to the small diameter of the channels, low mass flow rate and the thickness of the vane. The location of the cooling channels, especially near the trailing edge, is highly visible, showing the effect of this cooling mechanism. It is noticed that the cooling channels exhibit wave-like behaviour, which is a result of the thermal energy transferred from the mainstream to the coolant along the axial direction. On the pressure surface, it is noticed that low-temperature zones are formed following the leading edge. This is due to the profile of the vane, where the flow is fully developed, displaying a higher thermal resistance in these zones. As a final observation, steam is yet again proven to be the preferable cooling medium. In fact, the volume average temperature is 30 K lower when using steam.

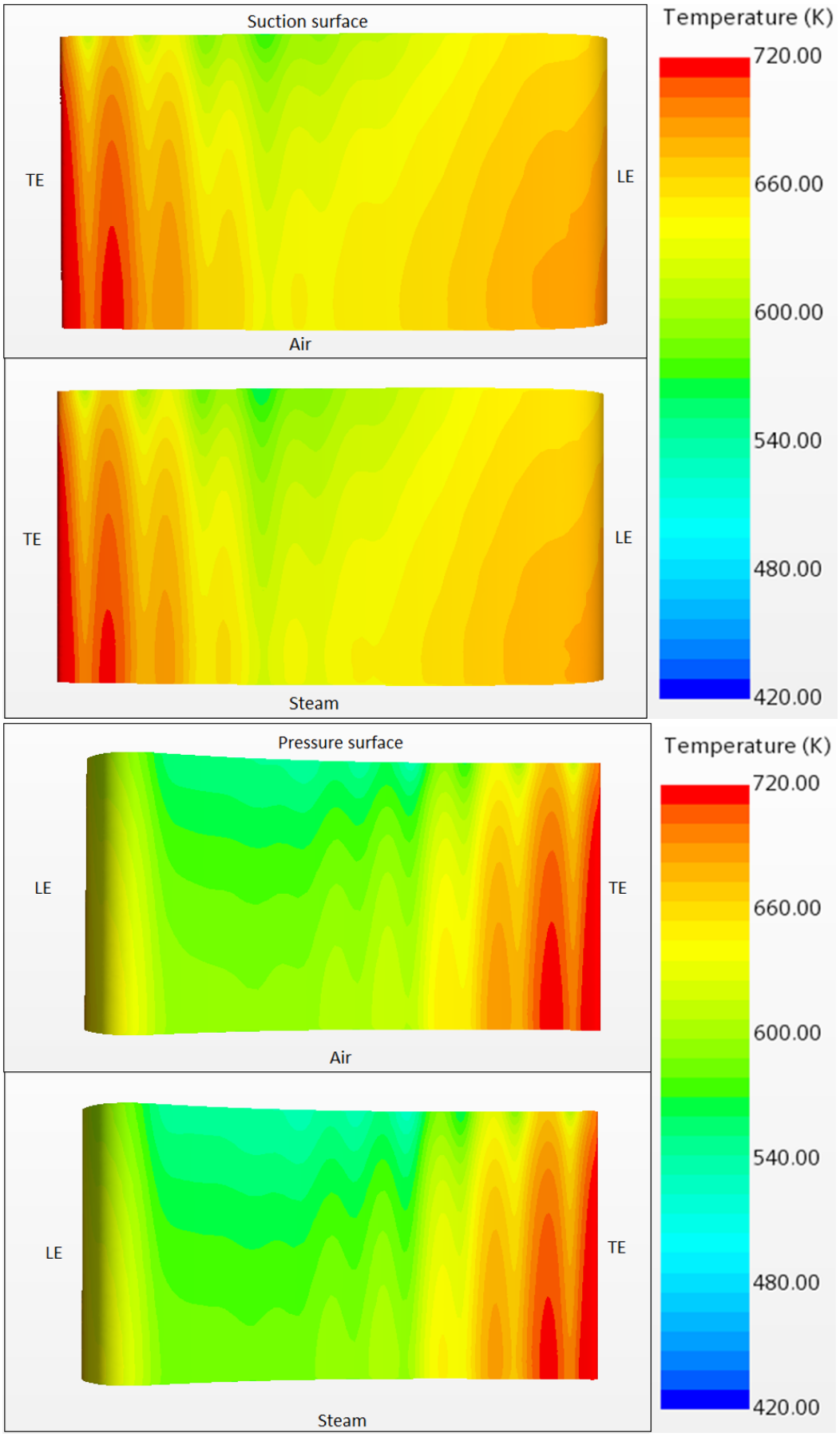

Fig. 5.9 Temperature contour comparison of the suction and pressure side.

Chapter 6

Summary and conclusion

3D conjugate heat transfer analyses have been performed on the radially cooled NASA C3X turbine guide vane, using the RANS based SST $k-\omega$ turbulence model. The objective was to evaluate the effects of steam as the cooling medium, which was compared against numerical results of air as coolant. The computational model was validated against experimental results, which used air as the cooling medium. [11]. Both the aerodynamic- and thermal characteristics were in good agreement with the experimental results, where the average relative difference was 1.39% and 3.78%, respectively.

Using the same boundary conditions, steam was proven to be the superior cooling medium, as expected. The temperature distribution of the two coolants displayed the same trends in the defined cross-sectional planes. Additionally, it was observed that the difference between the mediums increased along the axial direction of the vane. The average difference increased from 3.89% at the 25%-span to 5.29% at the 75%-span, which is equivalent to an increase of 13 K, solidifying steam as the preferable coolant.

Finally, it was shown that both the air- and steam cooled vane had some local areas with high temperatures. The inferior cooling effectiveness in these areas may lead to undesirable thermal loads and thermal stresses, contributing to a reduced lifespan of the vanes. Thus, further investigations are recommended to optimise the geometrical configuration and the mass flow rates of the cooling channels.

References

[1] A. Weaver, *Generation us: The challenge of global warming*. Orca Book Publishers, 2011.

[2] T.-M. Chen, W. G. Kuschner, J. Gokhale, and S. Shofer, "Outdoor air pollution: nitrogen dioxide, sulfur dioxide, and carbon monoxide health effects," *The American journal of the medical sciences*, vol. 333, no. 4, pp. 249–256, 2007.

[3] N. Sang, Y. Yun, H. Li, L. Hou, M. Han, and G. Li, "So2 inhalation contributes to the development and progression of ischemic stroke in the brain," *Toxicological Sciences*, vol. 114, no. 2, pp. 226–236, 2010.

[4] IEA, "Global energy review 2019."

[5] R. G. McKinney and J. B. Hoke, "Aero gas turbine combustion: Metrics, constraints, and system interactions," *Gas turbine emissions*, vol. 38, p. 3, 2013.

[6] V. McDonell and M. Klein, "Ground based gas turbine combustion: Metrics, constraints, and system interactions," *Gas Turbine Emissions*, vol. 38, p. 24, 2013.

[7] L. S. Langston, "Turbines, gas," *encyclopedia of Energy*, vol. 6, pp. 221–230, 2004.

[8] M. Konter and H. Bossmann, "Materials and coatings developments for gas turbine systems and components," in *Modern Gas Turbine Systems*, pp. 327–381e, Elsevier, 2013.

[9] T. Wang, "An overview of igcc systems," *Integrated Gasification Combined Cycle (IGCC) Technologies*, pp. 1–80, 2017.

[10] F. Montomoli, M. Carnevale, A. D'Ammaro, M. Massini, and S. Salvadori, *Uncertainty quantification in computational fluid dynamics and aircraft engines*. Springer, 2015.

[11] L. Hylton, M. Mihelc, E. Turner, D. Nealy, and R. York, "Analytical and experimental evaluation of the heat transfer distribution over the surfaces of turbine vanes," *Final Report Detroit Diesel Allison*, 1983.

[12] L. Hylton, V. Nirmalan, B. Sultanian, and R. Kaufman, "The effects of leading edge and downstream film cooling on turbine vane heat transfer," *Final Report General Motors Corp*, 1988.

[13] D. Bohn, U. Kruger, and K. Kusterer, "Conjugate heat transfer: an advanced computational method for the cooling design of modern gas turbine blades and vanes," *DEVELOPMENTS IN HEAT TRANSFER*, vol. 8, pp. 58–108, 2001.

[14] D. Bohn, T. Heuer, and K. Kusterer, "Conjugate flow and heat transfer investigation of a turbo charger," *J. Eng. Gas Turbines Power*, vol. 127, no. 3, pp. 663–669, 2005.

[15] W. D. York and J. H. Leylek, "Three-dimensional conjugate heat transfer simulation of an internally-cooled gas turbine vane," in *Turbo Expo: Power for Land, Sea, and Air*, vol. 36886, pp. 351–360, 2003.

[16] B. Facchini, A. Magi, and A. Scotti Del Greco, "Conjugate heat transfer simulation of a radially cooled gas turbine vane," in *Turbo Expo: Power for Land, Sea, and Air*, vol. 41685, pp. 951–961, 2004.

[17] S. M. Mousavi, A. Nejat, and F. Kowsary, "Optimization of turbine blade cooling with the aim of overall turbine performance enhancement," *Energy Equipment and Systems*, vol. 5, no. 1, pp. 71–83, 2017.

[18] P. Prapamonthon, S. Yooyen, S. Sleesongsom, D. Dipasquale, H. Xu, J. Wang, and Z. Ke, "Investigation of cooling performances of a non-film-cooled turbine vane coated with a thermal barrier coating using conjugate heat transfer," *Energies*, vol. 11, no. 4, p. 1000, 2018.

[19] J.-G. Bak, J. Cho, S. Lee, and Y. S. Kang, "Effects of inlet turbulence conditions and near-wall treatment methods on heat transfer prediction over gas turbine vanes," *International Journal of Aeronautical and Space Sciences*, vol. 17, no. 1, pp. 8–19, 2016.

[20] L. E. Bakken, K. Jordal, E. Syverud, and T. Veer, "Centenary of the first gas turbine to give net power output: A tribute to ægidius elling," in *Turbo Expo: Power for Land, Sea, and Air*, vol. 41677, pp. 83–88, 2004.

[21] E. W. Constant, *The origins of the turbojet revolution*. No. 5, Johns Hopkins University Press, 1980.

[22] P. Chiesa, G. Lozza, and L. Mazzocchi, "Using hydrogen as gas turbine fuel," *J. Eng. Gas Turbines Power*, vol. 127, no. 1, pp. 73–80, 2005.

[23] E. Global, "Hydrogen gas turbines: The path towards a zero-carbon gas turbine," *ETN Global*, p. 2, 2020.

[24] Y. A. Cengel and M. A. Boles, *Thermodynamics: An Engineering Approach 6th Editon (SI Units)*. The McGraw-Hill Companies, Inc., New York, 2007.

[25] M. P. Boyce, *Gas turbine engineering handbook*. Elsevier, 2011.

[26] S. Naik, "Basic aspects of gas turbine heat transfer," *Heat Exchangers–Design, Experiment and Simulation*, pp. 111–142, 2017.

[27] S. Ravelli and G. Barigozzi, "Numerical evaluation of heat/mass transfer analogy for leading edge showerhead film cooling on a first-stage vane," *International Journal of Heat and Mass Transfer*, vol. 129, pp. 842–854, 2019.

[28] B. Sunden and G. Xie, "Gas turbine blade tip heat transfer and cooling: a literature survey," *Heat Transfer Engineering*, vol. 31, no. 7, pp. 527–554, 2010.

[29] B. Andersson, R. Andersson, L. Håkansson, M. Mortensen, R. Sudiyo, and B. Van Wachem, *Computational fluid dynamics for engineers*. Cambridge university press, 2011.

[30] D. W. Hahn and M. N. Özisik, *Heat conduction*. John Wiley & Sons, 2012.

[31] T. Poinsot and D. Veynante, *Theoretical and numerical combustion*. RT Edwards, Inc., 2005.

[32] A. P. Wheeler, R. D. Sandberg, N. D. Sandham, R. Pichler, V. Michelassi, and G. Laskowski, "Direct numerical simulations of a high-pressure turbine vane," *Journal of Turbomachinery*, vol. 138, no. 7, 2016.

[33] P.-Y. Yu, W.-Y. Sean, R.-Y. Yeh, L.-H. C. Hsieh, R.-Q. Hsu, and T. Sato, "Direct numerical simulation of methane hydrate dissociation in pore-scale flow by using cfd method," *International Journal of Heat and Mass Transfer*, vol. 113, pp. 176–183, 2017.

[34] A. N. Kolmogorov, "The local structure of turbulence in incompressible viscous fluid for very large reynolds numbers," *Cr Acad. Sci. URSS*, vol. 30, pp. 301–305, 1941.

[35] J. Smagorinsky, "General circulation experiments with the primitive equations: I. the basic experiment," *Monthly weather review*, vol. 91, no. 3, pp. 99–164, 1963.

[36] W.-W. Kim and S. Menon, "A new dynamic one-equation subgrid-scale model for large eddy simulations," in *33rd Aerospace Sciences Meeting and Exhibit*, p. 356, 1995.

[37] M. Germano, U. Piomelli, P. Moin, and W. H. Cabot, "A dynamic subgrid-scale eddy viscosity model," *Physics of Fluids A: Fluid Dynamics*, vol. 3, no. 7, pp. 1760–1765, 1991.

[38] J. Delgadillo and R. Rajamani, "Hydrocyclone modeling: large eddy simulation cfd approach," *Mining, Metallurgy & Exploration*, vol. 22, no. 4, pp. 225–232, 2005.

[39] F. Fan, C. Wang, and J. Zhang, "Large eddy simulation of film cooling on turbine vane," *Journal of Thermal Science and Technology*, vol. 14, no. 2, pp. JTST0014–JTST0014, 2019.

[40] Y. Nagano and M. Tagawa, "An improved k-ε model for boundary layer flows," 1990.

[41] D. Rizzetta and D. Rizzetta, "Evaluation of algebraic reynolds-stress models for separated high-speed flows," in *28th Fluid Dynamics Conference*, p. 2125, 1997.

[42] P. R. Spalart, "Comments on the feasibility of les for wings, and on a hybrid rans/les approach," in *Proceedings of first AFOSR international conference on DNS/LES*, Greyden Press, 1997.

[43] P. Spalart and S. Allmaras, "A one-equation turbulence model for aerodynamic flows," in *30th aerospace sciences meeting and exhibit*, p. 439, 1992.

[44] M. Strelets, "Detached eddy simulation of massively separated flows," in *39th Aerospace sciences meeting and exhibit*, p. 879, 2001.

[45] W. M. Kays, "Turbulent prandtl number. where are we?," *ASME Transactions Journal of Heat Transfer*, vol. 116, no. 2, pp. 284–295, 1994.

[46] W. Jones and B. E. Launder, "The prediction of laminarization with a two-equation model of turbulence," *International journal of heat and mass transfer*, vol. 15, no. 2, pp. 301–314, 1972.

[47] D. C. Wilcox, "Reassessment of the scale-determining equation for advanced turbulence models," *AIAA journal*, vol. 26, no. 11, pp. 1299–1310, 1988.

[48] C. Argyropoulos and N. Markatos, "Recent advances on the numerical modelling of turbulent flows," *Applied Mathematical Modelling*, vol. 39, no. 2, pp. 693–732, 2015.

[49] F. R. Menter, "Two-equation eddy-viscosity turbulence models for engineering applications," *AIAA journal*, vol. 32, no. 8, pp. 1598–1605, 1994.

[50] S. Zheng, Y. Song, G. Xie, and B. Sunden, "An assessment of turbulence models for predicting conjugate heat transfer for a tubine vane with internal cooling channels," *Heat Transfer Research*, vol. 46, no. 11, 2015.

[51] STAR-CCM+, "User guide star-ccm+ version 2020.2.1."

[52] C. D. Rossman and M. A. Ricklick, "Analysis of a coupled micro-and triple-impingement cooling configuration in the c3x vane," in *52nd AIAA/SAE/ASEE Joint Propulsion Conference*, p. 4857, 2016.

[53] A. Goldsmith, *Handbook of thermophysical properties of solid materials*, vol. 5. Pergamon Press, 1963.

[54] F. M. White and I. Corfield, *Viscous fluid flow*, vol. 3. McGraw-Hill New York, 2006.

[55] A. Burcat, "Thermochemical data for combustion calculations," in *Combustion chemistry*, pp. 455–473, Springer, 1984.

[56] M. Peric and S. Ferguson, "The advantage of polyhedral meshes," *Dynamics*, vol. 24, no. 45, p. 504, 2005.

[57] T. Knopp, "Model-consistent universal wall-functions for rans turbulence modelling," in *International Conference on Boundary and Interior Layers, Göttingen, Germany*, Citeseer, 2006.

[58] K. C. Chitale, M. Rasquin, O. Sahni, M. S. Shephard, and K. E. Jansen, "Boundary layer adaptivity for incompressible turbulent flows," *arXiv preprint arXiv:1405.0620*, 2014.

[59] STAR-CCM+, "Installation guide star-ccm+ version 2020.2.1."

[60] A. Oliver, R. Lillard, A. Schwing, G. Blaisdell, and A. Lyrintzis, "Assessment of turbulent shock-boundary layer interaction computations using the overflow code," in *45th AIAA Aerospace Sciences Meeting and Exhibit*, p. 104, 2007.

[61] T. Jie and J. Jie, "Stress limiter consideration for k-omega turbulence models in shock-wave/turbulent boundary-layer interactions in supersonic and hypersonic flows," in *20th AIAA Computational Fluid Dynamics Conference*, p. 3980, 2011.

[62] G. S. Settles, *Schlieren and shadowgraph techniques: visualizing phenomena in transparent media*. Springer Science & Business Media, 2001.

[63] M. Wu and M. P. Martin, "Direct numerical simulation of supersonic turbulent boundary layer over a compression ramp," *AIAA journal*, vol. 45, no. 4, pp. 879–889, 2007.